Quarterly Technical Report

Solid State Research

1999:2

Lincoln Laboratory

MASSACHUSETTS INSTITUTE OF TECHNOLOGY

LEXINGTON, MASSACHUSETTS
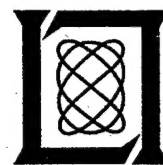
19990909 291

The ESC Public Affairs Office has reviewed this report, and it is releasable to the National Technical Information Service, where it will be available to the general public, including foreign nationals.

This technical report has been reviewed and is approved for publication.

FOR THE COMMANDER
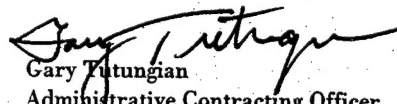
Gary Tutungian
Administrative Contracting Officer
Contracted Support Management

MASSACHUSETTS INSTITUTE OF TECHNOLOGY
LINCOLN LABORATORY

SOLID STATE RESEARCH

QUARTERLY TECHNICAL REPORT

1 FEBRUARY — 30 APRIL 1999

ISSUED 1 SEPTEMBER 1999

LEXINGTON   MASSACHUSETTS

ABSTRACT

This report covers in detail the research work of the Solid State Division at Lincoln Laboratory for the period 1 February through 30 April 1999. The topics covered are Quantum Electronics, Electro-optical Materials and Devices, Submicrometer Technology, Biosensor and Molecular Technologies, Microelectronics, Analog Device Technology, and Advanced Silicon Technology. Funding is provided by several DoD organizations—including the Air Force, Army, BMDO, DARPA, Navy, NSA, and OSD—and also by the DOE, NASA, and NIST.

TABLE OF CONTENTS

LIST OF ILLUSTRATIONS

LIST OF ILLUSTRATIONS (Continued)

LIST OF ILLUSTRATIONS (Continued)

LIST OF ILLUSTRATIONS (Continued)

LIST OF TABLES

xi

INTRODUCTION

1.   QUANTUM ELECTRONICS

High-power and high-efficiency optically pumped semiconductor lasers have been demonstrated that emit near 4 μm. Using 1.9-μm diode pump sources, we have achieved peak power outputs of ~1.6 W and net optical-to-optical power efficiencies as high as 10%.

2.   ELECTRO-OPTICAL MATERIALS AND DEVICES

Tapered-amplifier power splitters in which the signal is amplified during the splitting process have been fabricated. Gains in each output guide of a 1 × 8 splitter of 3.5–9.5 dB have been obtained at 1302 nm on initial devices.

3.   SUBMICROMETER TECHNOLOGY

A new method has been developed to measure the kinetic rate constant of the photoresist exposure reaction by using Fourier transform–infrared spectroscopy to track changes in the photoactive species. This new technique is well suited for use with opaque substrates and has been used to measure electron beam resists on chrome-coated quartz and silicon substrates.

An innovative microfluidic gas concentrator has been designed that uses thermophoresis to concentrate a preselected dilute constituent in air. When used in combination with a gas phase detector, such as an ion mobility spectrometer, the ability of the thermophoretic device to increase the concentration of the target constituent and to eliminate other interfering impurities will substantially increase the sensitivity of the resultant system over the detector alone.

4.   BIOSENSOR AND MOLECULAR TECHNOLOGIES

Cells that emit photons in response to antigen binding have been developed for a bioelectronic sensor project called CANARY (Cellular Analysis and Notification of Antigen Risks and Yields). Imaging and dose-response studies have been performed on monolayers of B cells attached to glass substrates, a format useful for incorporation into microfluidic biosensors.

5.   MICROELECTRONICS

An important issue in the design of high-frame-rate charge-coupled-device (CCD) imagers is charge carrier diffusion, which becomes the rate-limiting mechanism as the pixel-to-pixel well spacing increases. Simulated transient analysis of photogenerated carrier drift/diffusion effects was performed on shuttered and unshuttered CCD test structures to determine the photocarrier collection time vs collection well separation distances.

6.   ANALOG DEVICE TECHNOLOGY

Magnetically tunable superconducting filters consisting of microwave circuits coupled to ferrite substrates in monolithic structures using both niobium and YBCO have been demonstrated. A three-pole 1% bandwidth filter with 10-GHz center frequency is described, having insertion loss of 1 dB with niobium at 4 K, and 2 dB with YBCO at 77 K, and greater than 10% tunability.

7.   ADVANCED SILICON TECHNOLOGY

Digital circuit speeds approaching 2 GHz are reported in chips designed by the Mayo Foundation and fabricated in Lincoln's fully depleted silicon-on-insulator CMOS process. Speed is almost equal to that of a similar circuit fabricated in GaAs, but power dissipation is 40 times lower.

REPORTS ON SOLID STATE RESEARCH

1 FEBRUARY THROUGH 30 APRIL 1999

PUBLICATIONS

Semiconductor-Doped-Silica Saturable-Absorber Films for Solid-State Laser Mode Locking	I. P. Bilinsky[*] J. G. Fujimoto[*] J. N. Walpole L. J. Missaggia	*Opt. Lett.* **23**, 1766 (1998)
Critical Issues in 157 nm Lithography	T. M. Bloomstein M. Rothschild R. R. Kunz D. E. Hardy R. B. Goodman	*J. Vac. Sci. Technol. B* **16**, 3154 (1998)
Wide-Band Radiometry for Remote Sensing of Oil Films on Water	E. R. Brown[*] O. B. McMahon T. J. Murphy G. G. Hogan G. M. Daniels G. Hover[*]	*IEEE Trans. Microw. Theory Tech.* **46**, 1989 (1998)
InGaAsSb Thermophotovoltaic Diode: Physics Evaluation	G. W. Charache[*] P. F. Baldasaro[*] L. R. Danielson[*] D. M. DePoy[*] M. J. Freeman[*] C. A. Wang H. K. Choi D. Z. Garbuzov[*] R. U. Martinelli[*] V. Khalfin[*] S. Saroop[*] J. M. Borrego[*] R. J. Gutmann[*]	*J. Appl. Phys.* **85**, 2247 (1999)

[*]Author not at Lincoln Laboratory.

xv

Origin of Exchange Field Reductions in Diluted Magnetic Garnets	G. F. Dionne	*J. Appl. Phys.* **85**, 4627 (1999)
Magnetic Design for Low-Field Tunability of Microwave Ferrite Resonators	G. F. Dionne D. E. Oates	*J. Appl. Phys.* **85**, 4856 (1999)
High-Power 1.5-μm Tapered-Gain-Region Lasers	J. P. Donnelly J. N. Walpole S. H. Groves R. J. Bailey L. J. Missaggia A. Napoleone R. E. Reeder C. C. Cook	*Proc. SPIE* **3284**, 54 (1998)
Sub-100 nm KrF Lithography for Complementary–Metal–Oxide–Circuits	M. Fritze D. Astolfi H. Liu C. K. Chen V. Suntharalingam D. Preble P. W. Wyatt	*J. Vac. Sci. Technol. B* **17**, 345 (1999)
Bromine Ion-Beam-Assisted Etching of III-V Semiconductors	W. D. Goodhue Y. Royter D. E. Mull S. S. Choi C. G. Fonstad[*]	*J. Electron. Mater.* **28**, 364 (1999)
Microwave Power Handling in Engineered $YBa_2Cu_3O_{7-\delta}$ Grain Boundaries	Y. M. Habib[*] D. E. Oates G. Dresselhaus[*] M. S. Dresselhaus[*] L. R. Vale[*] R. H. Ono[*]	*Appl. Phys. Lett.* **73**, 2200 (1998)

---

[*]Author not at Lincoln Laboratory.

Ternary and Quaternary Antimonide Devices for Thermophotovoltaic Applications	C. W. Hitchcock[*] R. J. Gutmann[*] H. Ehsani[*] I. B. Bhat[*] C. A. Wang M. J. Freeman[*] G. W. Charache[*]	*J. Cryst. Growth* **195**, 363 (1998)
Excimer-Laser-Induced Densification of Fused Silica: Laser-Fluence and Material-Grade Effects on the Scaling Law	V. Liberman M. Rothschild J. H. C. Sedlacek R. S. Uttaro A. Grenville[*]	*J. Non-Cryst. Solids* **244**, 159 (1999)
A New RTD-FET Logic Family	R. H. Mathews J. P. Sage T. C. L. G. Sollner S. D. Calawa C-L. Chen L. J. Mahoney P. A. Maki K. M. Molvar	*Proc. IEEE* **87**, 596 (1999)
Hydride Vapor Phase Epitaxial Growth of III-V Nitrides	R. J. Molnar	In *Gallium Nitride (GaN) II*, J. I. Pankove and T. D. Moustakas, eds., Vol. 57 of *Semiconductors and Semimetals* (Academic, San Diego, 1999), Chap. 1
Resistive Arc Protection for Field-Emitter-Array Cold Cathodes Used in X-Band Inductive Output Amplifiers	L. Parameswaran C. T. Harris C. A. Graves R. A. Murphy M. A. Hollis	*J. Vac. Sci. Technol. B* **17**, 773 (1999)

[*]Author not at Lincoln Laboratory.

Generation and Detection of Coherent Terahertz Waves Using Two Photomixers	S. Verghese K. A. McIntosh S. D. Calawa W. F. Dinatale E. K. Duerr K. M. Molvar	*Appl. Phys. Lett.* **73**, 3824 (1999)
In Situ Monitoring of GaSb, GaInAsSb, and AlGaAsSb	C. J. Vineis C. A. Wang K. F. Jensen[*] W. G. Breiland[*]	*J. Cryst. Growth* **195**, 181 (1998)
Recent Progress in GaInAsSb Thermophotovoltaics Grown by Organometallic Vapor-Phase Epitaxy	C. A. Wang H-K. Choi D. C. Oakley G. W. Charache[*]	*J. Cryst. Growth* **195**, 347 (1998)
Contoured Elastic-Membrane Microvalves for Microfluidic Network Integration	A. M. Young T. M. Bloomstein S. T. Palmacci	*J. Biomech. Eng.* **121**, 2 (1999)
Mode-Discriminating Photoconductor and Coplanar Waveguide Circuit for Picosecond Sampling	N. Zamdmer[*] Qing Hu[*] S. Verghese A. Förster[*]	*Appl. Phys. Lett.* **74**, 1039 (1999)

ACCEPTED FOR PUBLICATION

Thermal Coefficients of the Expansion and Refractive Index in YAG	T. Y. Fan R. Wynne[*] J. Daneu	*Appl. Opt.*
PECVD Thin Films for MEMs Applications with Tailored Optical, Thermal, and Mechanical Properties	M. W. Horn R. B. Goodman M. Rothschild	*J. Vac. Sci. Technol. B*

[*]Author not at Lincoln Laboratory.

[*]Author not at Lincoln Laboratory.

PRESENTATIONS[†]

Non-epitaxial Semiconductor Doped Films for Laser Modelocking	J. N. Walpole L. J. Missaggia I. P. Bilinsky[*] R. P. Prasankumar[*] J. G. Fujimoto[*]	Advanced Solid State Lasers Topical Meeting, Boston, Massachusetts, 31 January–3 February 1999
Outlook for Resist Design at 157 nm	R. R. Kunz T. M. Bloomstein T. Fedynyshyn	157 nm Workshop, SEMATECH, Tuscon, Arizona, 7-9 February 1999
Theory and Experimental Results of New Diamond Surface-Emission Cathode	M. W. Geis N. Efremow, Jr. K. E. Krohn J. C. Twichell T. M. Lyszczarz	Technical Seminar, American Vacuum Society, Westboro, Massachusetts, 9 February 1999
A Nyquist-Rate Pipelined Oversampling A/D Converter	S. A. Paul D. Santiago T. Ala'ilma	Technical Seminar, ISSC, San Francisco, California, 15-17 February 1999
Detection of Contraband via Laser Ionization Ion Mobility Spectroscopy Using a Multi-megawatt Microchip Ultraviolet Laser	R. R. Kunz J. J. Zayhowski P. Becotte-Haigh[†] W. J. McGann[*]	Office of National Drug Control International Technology Symposium, Washington, D.C., 7-10 March 1999

---

[*]Author not at Lincoln Laboratory.

[†]Titles of presentations are listed for information only. No copies are available for distribution.

Magnetically Tunable Superconducting Filters	D. E. Oates A. C. Anderson G. F. Dionne	1999 Government Microcircuit Applications Conference, Monterey, California, 8-11 March 1999
Optical Materials and Coatings for 157-nm Lithography	T. M. Bloomstein V. Liberman D. E. Hardy R. Uttaro R. B. Goodman	
Thermomechanical Distortions of Advanced Optical Reticles During Exposure	J. Chang[*] A. Abdo[*] B. Kim[*] T. M. Bloomstein E. Lovell[*] W. Beckman[*] J. Mitchell[*]	24th SPIE International Symposium on Microlithography, Santa Clara, California, 11-15 March 1999
Screening of DNQ/Novolac Resists with E-Beam Exposure	T. H. Fedynyshyn S. P. Doran M. Lind T. M. Lyszczarz W. F. DiNatale D. M. Lennon C. Sauer[*] J. Muete[*]	
A FTIR Method to Determine Dill's C Parameter for DNQ/Novolac Resists with E-Beam and I-Line Exposure	T. H. Fedynyshyn S. P. Doran C. A. Mack[*]	

---

[*]Author not at Lincoln Laboratory.

---

[*]Author not at Lincoln Laboratory.

Metrology Methods for the Quantification of Line-Edge-Roughness II	C. Nelson S. C. Palmateer T. M. Lyszczarz A. R. Forte S. G. Cann S. J. Deneault	24th SPIE International Symposium on Microlithography, Santa Clara, California, 11-15 March 1999
Passively Q-Switched Microchip Lasers and Applications	J. J. Zayhowski	International Symposium on Advanced Technologies in Optical Communication and Sensing, Tokyo, Japan, 17-18 March 1999
Design of a Distributed Terahertz Photomixer	E. K. Duerr S. Verghese K. A. McIntosh	International Symposium on Space Terahertz Technologies, Charlottesville, Virginia, 17-19 March 1999
Passively Q-Switched Microchip Lasers and Applications	J. J. Zayhowski	R&D Institute for Photonic Engineering, Tokyo, Japan, 19 March 1999
Spectral Beam Combining of Yb-Doped Fiber Lasers in an External Cavity	C. C. Cook T. Y. Fan	Technical Seminar, Tufts University, Medford, Massachusetts, 2 April 1999
Theoretical and Experimental Study of a Low-Temperature Grown GaAs Photoconductive Switch under High Voltage Bias	S. Verghese K. A. McIntosh N. Zamdmer[*] Qing Hu[*]	1999 Optical Society of America Topical Meetings, Snowmass Village, Colorado, 4-16 April 1999

---

[*]Author not at Lincoln Laboratory.

Fast Vapor Concentrator	M. W. Geis R. R. Kunz	13th SPIE International Symposium on Aerospace/Defense Sensing, Simulation and Controls, Orlando, Florida, 5-9 April 1999
Photolithography at 193 nm	R. R. Kunz	Lincoln Laboratory Technical Seminar Series, Cornell University, Ithaca, New York, 13 April 1999
Optical Sampling for Analog to Digital Conversion	J. C. Twichell	DARPA/MTO PACT Kick Off Meeting, Lexington, Massachusetts, 20-21 April 1999
Theory and Experimental Results of a New Diamond Surface-Emission Cathode	M. W. Geis	Lincoln Laboratory Technical Seminar Series, Michigan State University, East Lansing, Michigan, 22 April 1999
Microchip Lasers	J. J. Zayhowski	Lincoln Laboratory Technical Seminar Series, Drexel University, Philadelphia, Pennsylvania, 26 April 1999
Ferrites for High Frequencies: Microwaves and Macrowaves	G. F. Dionne	Conference on Properties and Applications of Magnetic Materials, Chicago, Illinois, 26-28 April 1999
Optical Sampling for Analog to Digital Conversion	J. C. Twichell	Technical Seminar, Applied Technologies, Woburn, Massachusetts, 27 April 1999

ORGANIZATION

SOLID STATE DIVISION

D. C. Shaver, *Head*
R. W. Ralston, *Associate Head*
N. L. DeMeo, Jr., *Assistant*
Z. J. Lemnios, *Senior Staff*

J. W. Caunt, *Assistant Staff*
K. J. Challberg, *Administrative Staff*
J. D. Pendergast, *Administrative Staff*

SUBMICROMETER TECHNOLOGY

M. Rothschild, *Leader*
T. M. Lyszczarz, *Assistant Leader*
T. H. Fedynyshyn, *Senior Staff*
R. R. Kunz, *Senior Staff*

Astolfi, D. K.	Goodman, R. B.
Bloomstein, T. M.	Krohn, K. E.
Craig, D. M.	Liberman, V.
DiNatale, W. F.	Maki, P. A.
Doran, S. P.	Palmacci, S. T.
Efremow, N. N., Jr.	Palmateer, S. C.
Forte, A. R.	Sedlacek, J. H. C.
Geis, M. W.	Uttaro, R. S.

QUANTUM ELECTRONICS

A. Sanchez-Rubio, *Leader*
T. Y. Fan, *Assistant Leader*
T. H. Jeys, *Senior Staff*

Aggarwal, R. L.	DiCecca, S.
Buchter, S. C.	Goyal, A. K.
Cook, C. C.	O'Brien, P. W.
Daneu, J. L.	Ochoa, J. R.
Daneu, V.	Zayhowski, J. J.

ELECTRO-OPTICAL MATERIALS AND DEVICES

D. L. Spears, *Leader*
J. C. Twichell, *Assistant Leader*
G. W. Turner, *Assistant Leader*
H. K. Choi, *Senior Staff*
R. C. Williamson, *Senior Staff*

Bailey, R. J.	Juodawlkis, P. W.	Nitishin, P. M.
Betts, G. E.	Liau, Z. L.	Oakley, D. C.
Calawa, A. R.*	Lightfoot, A.	O'Donnell, F. J.
Calawa, D. R.	Mahoney, L. J.	Poillucci, R. J.
Calawa, S. D.	Manfra, M. J.	Reeder, R. E.
Connors, M. K.	McIntosh, K. A.	Taylor, P. J.
Donnelly, J. P.	Missaggia, L. J.	Verghese, S.
Goodhue, W. D.	Molnar, R. J.	Walpole, J. N.
Harman, T. C.	Mull, D. E.	Wang, C. A.
Harris, C. T.	Napoleone, A.	Wasserman, J. L.

---

*Part Time

xxvi

1. QUANTUM ELECTRONICS

1.1 HIGH-POWER, HIGH-EFFICIENCY MID-INFRARED SEMICONDUCTOR LASERS

Many military, industrial, and medical applications require laser systems with high peak and/or average power in the mid-infrared (3–5 μm) region of the spectrum. A popular approach to the problem has been to generate the radiation with an optical parametric oscillator pumped with a near infrared laser. However, this technique is inherently complex and difficult to make into a robust system. We have developed InAsSb double-heterostructure (DH) optically pumped semiconductor lasers that provide high peak and average powers near 4 μm with high efficiency. In addition, systems of this type can potentially be simple, compact, and robust.

The DH lasers consist of an InAsSb active region combined with AlAsSb cladding regions. The InAsSb and AlAsSb layers are grown nominally lattice matched on (100)-oriented n-GaSb substrates by solid-source molecular-beam epitaxy. A typical laser structure consisted of the following layers: 0.5-μm GaSb buffer, 2-μm AlAs(0.08)Sb(0.92) cladding, 1.5-μm InAs(0.91)Sb(0.09) active region, 2-μm AlAs(0.08)Sb(0.92) cladding, and 0.01-μm GaSb cap. After growth, the wafers are thinned to ~100 μm and cleaved into samples. The lasers are optically pumped with a three-bar stack of 1.9-μm diode laser arrays with integrated collimating lenses capable of providing a combined output of more than 20-W peak power. The pump conditioning optics provide a ~100-μm-wide by 2.2-mm-long pump stripe at the DH laser chip. The chip is housed in a dewar and cooled to ~82 K with liquid nitrogen.

Previous efforts at lower pump power have achieved net optical-to-optical power efficiencies of 6.5% [1]. Through developments in three key areas, we have been able to demonstrate power efficiencies of 10% at low pump powers (<10-W peak) and 8% at high power (>20-W peak). First, improvements in the laser facet high-reflection (HR) and antireflection (AR) coatings increased the single-ended coupling efficiency. A change in coating geometry increased the reflectivity of the gold HR coating while a systematic optimization of layer thickness decreased the reflectivity of the dielectric AR coating. By measuring the performance of the laser without facet coatings and then after each coating step, we have determined the effective reflectivities of the HR and AR coatings to be 90 and 9%, respectively. Low-reflectivity AR coatings are an exceptionally difficult problem owing to the long wavelength, broad bandwidth, and large angular acceptance requirements. Second, the pumping conditions have been thoroughly evaluated and an optimum configuration has been implemented. Characterization of the chip emission properties (beam quality) as a function of pump beam geometry has allowed for the maximum power to be collected in a usable output beam. Finally, new techniques for thermal management have been developed allowing the lasers to be run at high average pump powers. The laser chips are mounted with the active region contacted to a diamond heat spreader. The diamond is then mounted on a larger copper thermal mass. This arrangement has allowed average output powers of up to 400 mW at 25% duty cycle. A typical graph of laser performance is shown in Figure 1-1. As can be seen, however, thermal rollover is still an issue. Experiments to determine the contributions to the decrease in efficiency due to intrapulse and average power heating are in progress.
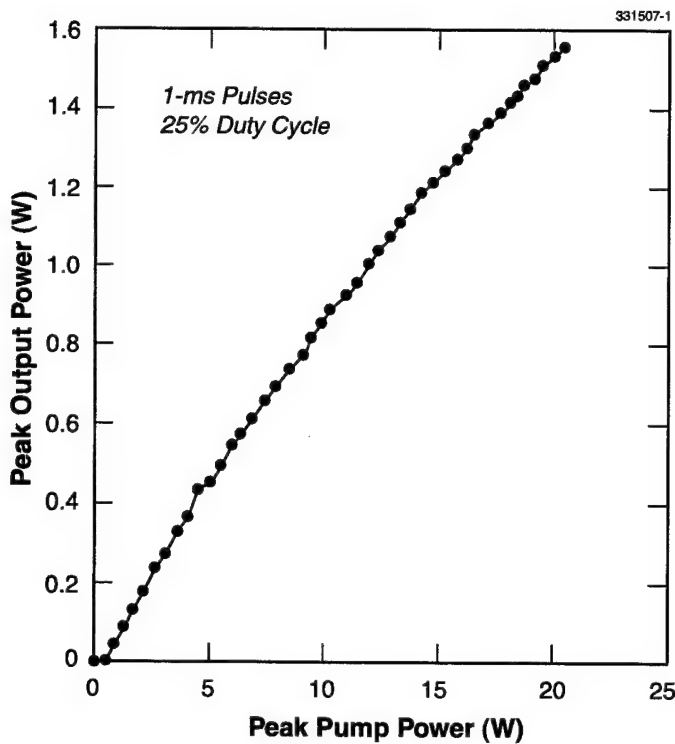
Figure 1-1. 4-μm peak output power vs 1.9-μm peak pump power.

In conclusion, we have demonstrated optical-to-optical conversion efficiencies as high as 10% with our laser systems. Further improvements in previously mentioned areas are in progress. New diagnostics to examine the chip emission properties have been implemented, which should allow further advances in facet coatings as well as pump beam geometry. Work is also concentrated on improving the intrinsic properties of the 4-μm semiconductor laser materials.

S. C. Buchter	J. R. Ochoa
C. C. Cook	J. L. Daneu
G. W. Turner	A. Sanchez
H. K. Choi	P. Foti

REFERENCE

1.   H. Q. Le, G. W. Turner, and J. R. Ochoa, *IEEE Photon. Technol. Lett.* **10**, 663 (1998).

2. ELECTRO-OPTICAL MATERIALS AND DEVICES

2.1 ALL-ACTIVE InGaAsP/InP OPTICAL TAPERED-AMPLIFIER $1 \times N$ POWER SPLITTERS

Photonic and optoelectronic systems require semiconductor optical amplifiers, splitters, and switches with high speed, bandwidth, and gain. Various passive and active splitter and combiner designs have been proposed for optoelectronic systems [1]–[4]. Trees of Y-branches, two-dimensional (2D) free-space diffraction region devices with input and output guide coupling, and multimode-waveguide imaging devices have all been proposed as passive splitters [1]. Passive power splitters require pre- and/or post-amplification to compensate for the splitting loss. For $1 \times N$ splitters with large N, power saturation effects in single-mode amplifiers limit preamplification, and therefore postamplification is usually also required. Postamplification, however, only adds more noise and does nothing to alleviate the signal-to-noise-ratio degradation that occurs during the $1 \times N$ passive splitting process. Amplification during the splitting process can prevent this signal-to-noise ratio degradation and result in signal-to-noise ratios similar to preamplification without the power saturation effects inherent in an input single-mode amplifier. All-active trees of Y-branches are possible and have been proposed but are difficult to scale to large N. Amplification in a multimode-waveguide splitter turns out to be essentially the same as postamplification. Extremely tight tolerances on index, geometry, and wavelength in multimode devices also limit the robustness of this type of splitter. Tapered-amplifier 2D diffraction splitters, however, are both scalable and robust, and preserve most of the signal-to-noise advantages of amplifying during the splitting process. Here, we present the design, fabrication, and testing of tapered-amplifier power splitters.

A schematic of the 1×8 all-active tapered-amplifier power splitter (TAPS) is illustrated in Figure 2-1. There are three main sections to the TAPS design. The first section is a single-mode ridge waveguide that serves as a preamplifier. The single-mode input section also provides a well-defined input to the 2D diffracting region and therefore determines the diffraction pattern in this region. A tapered amplifier in the diffraction region that is designed to match the diffracting pattern amplifies the signal during diffraction and keeps the signal intensity high. The active output waveguides are apodized to obtain approximately equal signal powers in each of the output waveguides. This apodization results in a slightly lower signal to noise in the outer guides compared to the center guides, but it is still superior to postamplification. All of the output guides are adiabatically tapered down and the S-bends are used to route the outputs to the straight single-mode output waveguides, as indicated in Figure 2-1. Although the results presented here on an all-active TAPS device are for all sections driven in parallel, the individual sections can be driven separately. In this case, the outputs can be used as ON/OFF switches as well as amplifiers.

The material used to fabricate the TAPS devices is a separate-confinement heterostructure with three InGaAsP quantum wells under 1% compressive strain that was grown by organometallic vapor-phase epitaxy. The p-type InP upper cladding layer contains an "etch stop" layer to facilitate the fabrication of the ridge waveguides. A top p^+-InGaAs layer is provided to facilitate p-type ohmic contact formation. The waveguides are fabricated using CH_4/H_2 reactive ion etching followed by a short selective wet-chemical etch which stops at the etch stop layer. The titanium etch mask used for the reactive ion etching is removed

331507-2
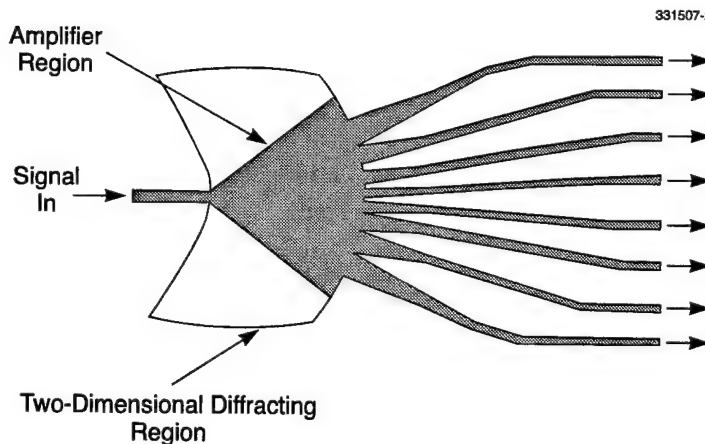
Figure 2-1. Schematic of an all-active 1 × 8 tapered-amplifier power splitter (TAPS) device with the gray area depicting the metallization

and a dielectric layer deposited. Standard photolithography and etching techniques are then performed to provide contact openings in the dielectric layer. A Ti-Pt-Au metallization is used to form the ohmic contact to the p^+-InGaAs layer. The top contacts are segmented to allow separate excitation of the input ridge, the 2D horn, and the output splitters in the future. The wafer is thinned and then a back side Ni-Ge-Au contact is applied to the n^+-InP substrate. The devices are cleaved and mounted junction side down on a Cu package, and both facets are antireflection coated with a single layer of silicon monoxide.

In the devices reported here, the input and output ridge waveguides are 2.5 μm wide. The 1 × 8 splitters have a 2D diffraction region with a radius of 500 μm and an output guide separation of 30 μm. The 1 × 16 splitters have a 2D diffraction region with a radius of 1000 μm and an output guide separation of 20 μm.

To test the splitter design, passive 1 × 8 and 1 × 16 devices were fabricated in a passive-waveguide growth to match the active-waveguide device characteristics. The 1 × 16 passive devices have output power uniformity from guide to guide of better than ±4% around the average output power, as seen in Figure 2-2. The 1 × 8 devices have uniformity of ±9%. The total insertion loss (total output power in all output guides divided by input power) was around −1.8 dB.

The active TAPS devices are mounted on a thermoelectric cooler to keep the temperature at 20°C. For the gain measurement, the chopped input beam from a Fabry-Perot laser diode operating at a wavelength of 1305 nm is coupled into the input ridge of the TAPS device with a 20× objective lens. A reversed-bias photocurrent measurement is used to determine the power coupled into the device. The output of the device was magnified so each output waveguide could be imaged individually on a calibrated photodiode. Chopping the input signal facilitates separating the amplified signal from the amplified spontaneous emission.

4
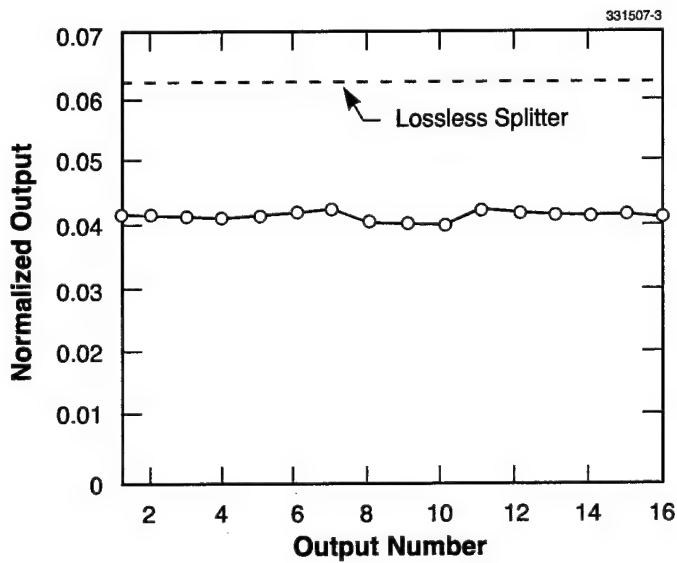
Figure 2-2. Normalized output power of each guide of a 1 × 16 passive splitter.

The measured output powers of a 1 × 8 TAPS device with a coupled input power of 350 μW along with a photograph of the output near-field pattern are shown in Figure 2-3. In this case, all sections are driven in parallel at a current of 1.85 A. Gain in the output guides ranged from 9.5 dB for the center guides to 3.5 dB for the lowest outside guide. The uniformity is not as good as obtained for the passive splitters. The outputs of guides 1 and 2, in particular, are substantially less than the center guides. Uniformity appeared better at lower drive currents and under pulsed conditions, indicating that some of the problem may be associated with nonuniform soldering resulting in nonuniform current distribution and junction temperature.

We have presented initial results on all-active TAPS devices. Gains in each output guide ranged from 3.5 to 9.5 dB at a drive current of 1.85 A. Uniformity of the outputs can be improved by increasing the input guide's lateral confinement. This will decrease the input mode width and increase the diffraction angle to better fill the taper section. Uniformity should also be improved with better soldering and mounting. Operating currents can be decreased by material improvements and by driving the individual sections independently. The devices reported here were fabricated from material that has a transparency current density of 270 A/cm. This is substantially higher than our more typical laser material, which with the same structure has a transparency current density in the vicinity of 150 A/cm^2. Both 1 × 8 and 1 × 16

Guide Number	Output Power (mW)
1	0.81
2	1.10
3	1.92
4	3.15
5	3.15
6	2.72
7	2.04
8	1.62

(a)
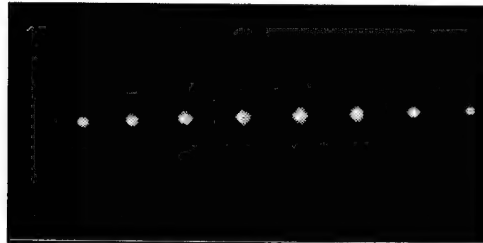
(b)

Figure 2-3. (a) Output power of each output guide of 1 × 8 power splitter with 350 µW of coupled input power. (b) Photograph of the near-field pattern of the output of the splitter.

devices are currently being fabricated with higher-quality material. Improvements are also expected by operating at a wavelength that more optimally matches the gain spectra of the devices and by improvements in the antireflective coatings.

S. S. Choi   J. P. Donnelly
S. H. Groves   R. E. Reeder
R. J. Bailey   P. J. Taylor
W. D. Goodhue

REFERENCES

1. F. Ratovelomanana, N. Vodjdani, A. Enard, G. Glastre, D. Rondi, and R. Blondeau, *IEEE Photon. Technol. Lett.* **7**, 511 (1995).

2. M. Zirngibl, C. Dragone, C. H. Joyner, M. Kuznetsov, and U. Koren, *Electron. Lett.* **28**, 1212 (1992).

3. U. Koren, M. G. Young, B. I. Miller, M. A. Newkirk, M. Chien, M. Zirngibl, C. Dragone, B. Glance, T. L. Koch, B. Tell, K. Brown-Goebeler, and G. Raybon, *Appl. Phys. Lett.* **61**, 1613 (1992).

4. M. G. Young, U. Koren, B. I. Miller, M. A. Newkirk, M. Chien, M. Zirngibl, C. Dragone, B. Tell, H. M. Presby, and G. Raybon, *IEEE Photon. Technol. Lett.* **5**, 908 (1993).

3. SUBMICROMETER TECHNOLOGY

3.1 A FT-IR SPECTROSCOPY METHOD TO DETERMINE THE DILL PARAMETER FOR LITHOGRAPHY MODELING

Lithography simulation has become an important tool for research, development, and manufacturing applications in semiconductor fabrication [1]. In many cases the accuracy of such simulation is limited not so much by the models themselves as by the accuracy of the input parameters used by the models. One such parameter is the kinetic rate constant of the first-order exposure reaction of a photoresist, the so-called Dill C parameter [2]. A photosensitive component of the photoresist, called a photoactive compound (PAC) or a photoacid generator (PAG), undergoes a first-order photochemical decomposition to some product (typically an acid) as a function of E, the dose incident on the PAC molecules:

$$\frac{\partial m}{\partial E} = -Cm \tag{3.1}$$

where m is the relative concentration of the photosensitizer and C is the exposure rate constant [1],[2]. Note that the exposure dose E represents the dose incident on the PAC molecules themselves and may not be equal to the dose incident on the top of a thin film of photoresist. Equation (3.1) has an obvious solution:

$$m = e^{-CE} \tag{3.2}$$

Measurement of the Dill C parameter typically involves measurement of some physical quantity directly proportional to m as a function of incident dose. Then, using simulation to convert incident dose to actual dose, a best fit of Equation (3.2) to the data yields the rate constant C [3]. The most common measurement technique for optical resists, first proposed by Dill, is to measure the absorbance of the resist film at the actinic wavelength *in situ* during exposure. Changes in m are directly proportional to changes in the absorbance. However, resist absorbance at the actinic wavelength may not be selective in isolating and measuring only the photoactive species, and in some cases changes in absorbance cannot be directly correlated to changes in the concentration of the photoactive species. Fourier transform–infrared (FT-IR) spectroscopy can directly measure changes in the photoactive species by isolating and measuring absorbance peaks unique to the photoactive species. FT-IR spectroscopy, by employing reflectance mode measurement, is not constrained to transparent substrates, but can instead be used with silicon wafers or chrome-coated quartz plates. The ability to use these substrates is important when determining the Dill C parameter under e-beam exposure, where the degree of back-scattered electrons is dependent on the underlying substrate, and the use of quartz is prohibited because of charging considerations.

We employed the FT-IR spectroscopy method to determine the Dill C parameter for a variety of commercial i-line resists under e-beam exposure. All diazonaphthoquinone (DNQ)/novolac resists contain a diazide moiety on the PAC species, and it is this diazide functionality that initiates the photochemical

rearrangement that transforms the DNQ to an indene carboxylic acid. The diazide moiety has a unique infrared absorbance at about 2100 cm^{-1} that can be easily monitored with little interference from other PAC or polymer functionality. A typical FT-IR spectrum of a DNQ/novolac resist showing the change in the absorbance at ~2100 cm^{-1} as a function of exposure time is seen in Figure 3-1. Illumination was with the white light illuminator of the microscope and is given in seconds. The spectra shown are the difference of the spectra taken at different exposure times subtracted from the unexposed spectra. The scale is adjusted for clarity to show the *absolute value* of the change in absorbance. During exposure the absorbance between 2045 and 2206 cm^{-1} decreases, reflecting a decrease in DNQ concentration.

A typical experiment to determine the Dill C parameter was to coat a wafer with 600 nm of resist and expose a dose matrix. The normalized IR absorbency as a function of exposure dose was determined and the best fit of Equation (3.2) yielded the Dill C value in terms of cm^2/μC. An example of the decrease in IR absorbance as a function of exposure dose for SPR700 with e-beam exposure on a chrome-coated silicon dioxide wafer is presented in Figure 3-2. All resists gave similar plots with very good fits to Equation (3.2). Values for C measured on chrome on quartz substrates are presented in Table 3-1 both in units of cm^2/μC, the traditional units associated with the Dill C parameter, and in units of cm^3/J, the latter accounting for the absorbed dose within the resist [4]. The conversion factor from cm^2/μC to cm^3/J was determined by calculating the average deposited dose in the resist via Pro Beam/3D, an e-beam lithography simulator [4].

The Dill C value in terms of incident dose ranges from 0.0061 to 0.0092 cm^2/μC for the seven resists measured, although most resists fall in a relatively small range from 0.0070 to 0.0079 cm^2/μC. It is not clear why the Dill C parameters for the Shipley and Clariant resists are significantly lower and higher, respectively, than the values observed for the remaining five resists which all cluster rather tightly. The

331507-5
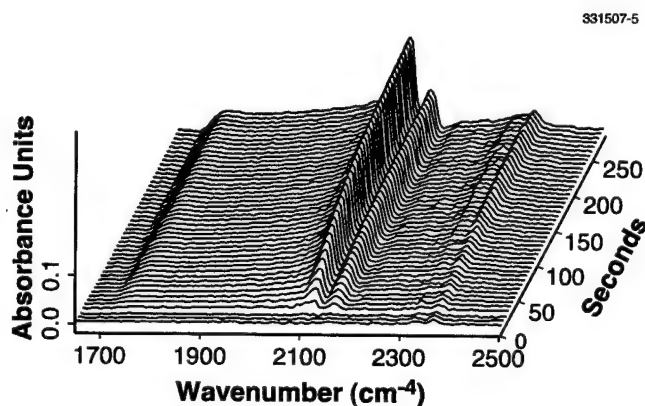
Figure 3-1. Typical Fourier transform–infrared (FT-IR) spectrum of diazonaphthoquinone (DNQ)/novolac resist showing the change in absorbance at ~2100 cm^{-1} as a function of exposure time. Illumination was with the white light illuminator of the microscope and is given in seconds. The scale is adjusted for clarity to show the <u>absolute value</u> of the change in absorbance. During exposure the absorbance between 2045 and 2206 cm^{-1} decreases, reflecting a decrease in DNQ concentration.

331507-6
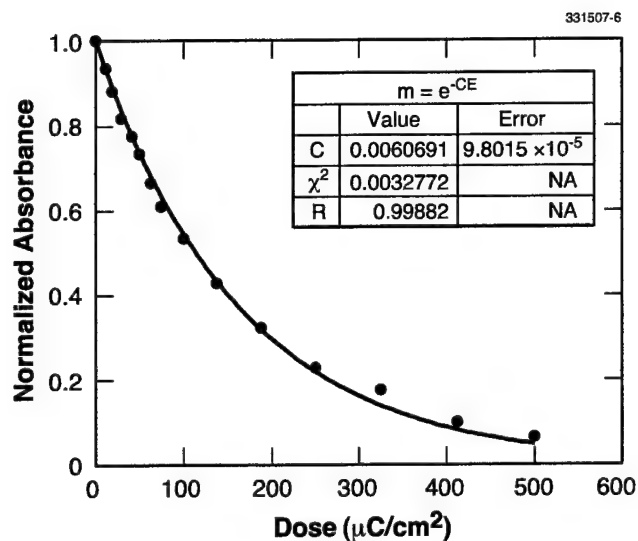
Figure 3-2. Determining the Dill C parameter for SPR700 on chrome-coated silicon dioxide substrate by plotting normalized DNQ absorbance as a function of 50-kV e-beam exposure dose and obtaining the fit to the equation $m = e^{-CE}$.

TABLE 3-1
Dill C Parameters Determined for DNQ/Novolac Resists Exposed with a 50-kV Electron Beam on a Chrome-Coated Silicon Dioxide Substrate*

Manufacturer	Resist	Dill C $(cm^2/\mu C)$	Error $(cm^2/\mu C)$	Dill C (cm^3/J)
Clariant	AZ5204	0.0092	± 0.00012	0.00133
JSR	IX420H	0.0072	± 0.00013	0.00106
Olin	OiR 907-12	0.0073	± 0.00014	0.00110
Shipley	SPR700	0.0061	± 0.00010	0.00097
Sumitomo	PFM-10A4	0.0070	± 0.00014	0.00106
TOK	OEBR2000	0.0079	± 0.00014	0.00116
Nippon Zeon	ZMP	0.0070	± 0.00011	0.00103

*The Dill C is determined by a best fit to the equation $m = e^{-CE}$.

standard error associated with determining the Dill C value on chrome-coated silicon dioxide is quite low and ranges from 1 to 2% for all seven resists. This small error allows one to say with confidence that the Shipley and Clariant resists show different PAC decomposition behavior than the other resists with e-beam exposure.

Two other substrates were employed to determine the e-beam Dill C parameter for the seven i-line resists. An example of the decrease in IR absorbance as a function of exposure dose for SPR700 with e-beam exposure on an aluminum-coated silicon wafer is presented in Figure 3-3. All resists gave similar plots with very good fits. Values for C measured on aluminum on silicon substrates are presented in Table 3-2 in both units of $cm^2/\mu C$ and cm^3/J.

The Dill C value in terms of incident dose ranges from 0.0069 to 0.0095 $cm^2/\mu C$ for the seven resists measured, although most resists fall in a relatively small range from 0.0073 to 0.0080 $cm^2/\mu C$. Like the chrome on silicon dioxide results, the Dill C parameters for the Shipley and Clariant resists are significantly lower and higher, respectively, than the values observed for the remaining five resists, which all cluster rather tightly. The standard error associated with determining the Dill C value on chrome-coated silicon dioxide again is quite low and ranges from 1 to 2% for all seven resists. As expected, comparison of the values in Tables 3-1 and 3-2 shows that the extracted C values do not show a discernible substrate dependence.

The final substrate employed to determine the Dill C parameter for the seven i-line resists was bare silicon. An example of the decrease in IR absorbance as a function of exposure dose for SPR700 with e-beam exposure on a silicon wafer is presented in Figure 3-4. All resists gave similar plots with relatively poor fits. Values for C measured on silicon substrates are presented in Table 3-3 in both units of $cm^2/\mu C$ and cm^3/J.

The Dill C value in terms of incident dose ranges from 0.0057 to 0.0088 $cm^2/\mu C$ for the seven resists measured with none of the tight clustering of values seen on chrome or aluminum. The standard error associated with determining the Dill C value on silicon is much higher compared to the other two substrates and ranges from 5 to 25% for the seven resists. This large error is due in part to the poor fit at higher exposure doses when most of the PAC has decomposed. Silicon, unlike chrome and aluminum, is not highly reflective in the IR. Instead, some of the IR is transmitted through the silicon and is subsequently reflected by the metal microscope stage. This reflection sets up IR standing waves in the silicon and also the coated resist, causing interference in measuring low PAC values. This is due to difficulty in assigning a reference absorbance as well as integrating the standing waves along with the actual IR absorbance. This interference is not seen with substrates, such as chrome and aluminum, which do not transmit in the IR and as such are preferred for determining PAC concentration by this method.

T. H. Fedynyshyn
S. P. Doran
C. A. Mack*
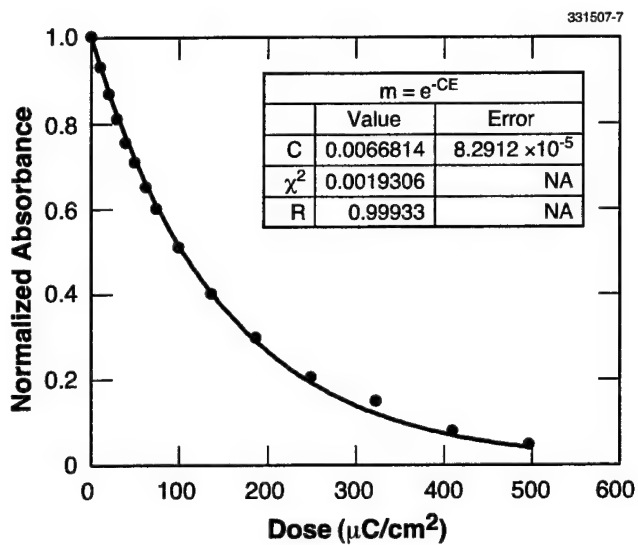
Figure 3-3. Determining the Dill C parameter for SPR700 on aluminum-coated silicon substrate by plotting the normalized DNQ absorbance as a function of 50-kV e-beam exposure dose and obtaining the fit to the equation $m = e^{-CE}$.

TABLE 3-2
Dill C Parameters Determined for DNQ/Novolac Resists Exposed with a
50-kV Electron Beam on an Aluminum-Coated Silicon Substrate*

Manufacturer	Resist	Dill C ($cm^2/\mu C$)	Error ($cm^2/\mu C$)	Dill C (cm^3/J)
Clariant	AZ5204	0.0095	± 0.00014	0.00143
JSR	IX420H	0.0073	± 0.00013	0.00110
Olin	OiR 907-12	0.0076	± 0.00011	0.00115
Shipley	SPR700	0.0069	± 0.00008	0.00104
Sumitomo	PFM-10A4	0.0073	± 0.00012	0.00110
TOK	OEBR2000	0.0080	± 0.00009	0.00121
Nippon Zeon	ZMP	0.0071	± 0.00008	0.00107
*The Dill C is determined by a best fit to the equation $m = e^{-CE}$.				

331507-8

$m = e^{-CE}$		
	Value	Error
C	0.0083168	0.0006359
χ^2	0.07291	NA
R	0.97074	NA
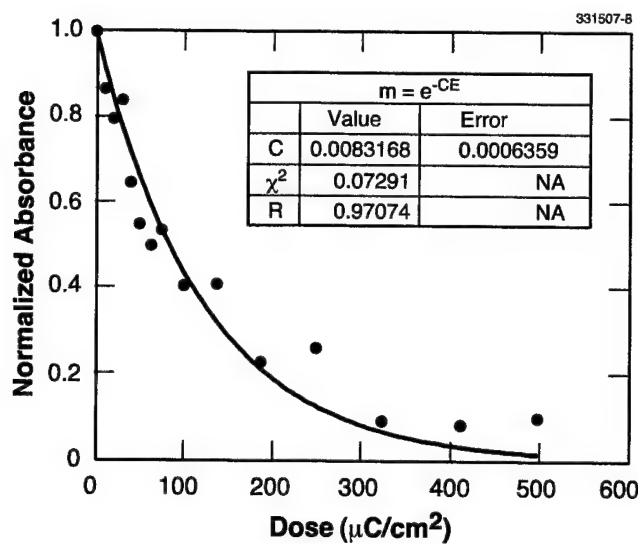
*Figure 3-4. Determining the Dill C parameter for SPR700 on silicon substrate by plotting normalized DNQ absorbance as a function of 50-kV e-beam exposure dose and obtaining the fit to the equation $m = e^{-CE}$.*

TABLE 3-3
Dill C Parameters Determined for DNQ/Novolac Resists Exposed with a
50-kV Electron Beam on a Silicon Substrate*

Manufacturer	Resist	Dill C ($cm^2/\mu C$)	Error ($cm^2/\mu C$)	Dill C (cm^3/J)
Clariant	AZ5204	0.0088	± 0.00050	0.00128
JSR	IX420H	0.0075	± 0.00182	0.00109
Olin	OiR 907-12	0.0083	± 0.00064	0.00121
Shipley	SPR700	0.0083	± 0.00064	0.00121
Sumitomo	PFM-10A4	0.0057	± 0.00055	0.00083
TOK	OEBR2000	0.0081	± 0.00090	0.00118
Nippon Zeon	ZMP	0.0070	± 0.00159	0.00102

*The Dill C is determined by a best fit to the equation $m = e^{-CE}$.

14

3.2 DESIGN OF A CHEMICAL CONCENTRATOR FOR RAPID VAPOR DETECTION

There are numerous applications in process control, environmental monitoring, and drug and explosive detection for sensors capable of detecting minute quantities of gaseous materials. In most gas sensors, the minimum detectable level of a target compound is limited not by the inherent sensitivity of the sensor, but by false positives and interference from other gaseous constituents. The ability to selectively preconcentrate an arbitrary dilute constituent by several orders of magnitude and to eliminate background impurities prior to subsequent downstream detection increases the sensor sensitivity in a field environment. This report describes the design of an innovative gas concentrator that uses thermophoresis to concentrate a preselected dilute constituent in air.

In 1872, Dufour [5] reported that when two gases are allowed to diffuse together a transient temperature gradient results. Similarly, when a temperature gradient is applied to a homogeneous mixture of two gases or liquids a concentration gradient results. A concentration gradient driven by a thermal gradient is referred to as thermal diffusion or the Soret effect. As a result of the derivation of the Boltzmann equation for dense gases in the early 20th century by Enskog [6] and Chapman et al. [7],[8], it became apparent that dilute constituents, atoms, molecules, or particles in a carrier gas could be concentrated by thermal gradients. From this realization a variety of thermal techniques have been developed and used to separate isotopes. Two cases in particular are of interest. When the molecular or particle constituents are larger or heavier than the carrier gas molecules, the constituents in the thermal gradient will move from the hotter to the colder regions. In this case, the carrier gas molecules from the hotter region impart more momentum to the dilute constituents than the carrier gas molecules from the colder region. On the other hand, constituents that are smaller and lighter than the carrier gas molecules are driven to the hotter region, as depicted in Figure 3-5.

Two experimental conditions for a dilute constituent in a thermal gradient will be considered. The first condition exists when a thermal gradient is impressed on a gas mixture in a closed container, as shown in Figure 3-5(b). The constituents thermophoretically diffuse until an equilibrium concentration is

331507-9

25°C	25°C	200°C	25°C
(a)		**(b)**	
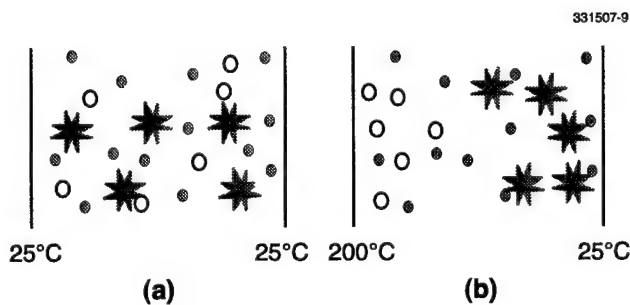
Figure 3-5. (a) Gaseous constituents are uniformly mixed at constant temperature. (b) Thermal gradient causes constituents to separate. Solid circles represent the carrier gas, air or nitrogen; open circles represent a constituent of lower molecular weight; and stars represent a constituent of higher molecular weight.

15

reached. The partial pressure ratio R of a constituent is dependent upon the high and low temperatures in the container, T_{High} and T_{Low}, and the thermophoresis coefficient α_{12},

$$R = \frac{X_{Low}}{X_{High}} = \left[\frac{T_{Low}}{T_{High}}\right]^{\alpha_{12}}$$

(3.3)

where X_{High} is the ratio of the partial pressure of the constituent to the total pressure in the high-temperature region and X_{Low} is the ratio of the partial pressure of the constituent to the total pressure in the low-temperature region. A temperature difference of a few hundred degrees Celsius in a carrier gas of nitrogen will cause low molecular weight gases, like hydrogen, to increase in partial pressure by ~10% in the higher-temperature region, while impurities with molecular weights larger than nitrogen can increase their partial pressure by more than 100% in the cooler regions. The concentration increase between the cooler and hotter regions for several dilute constituents in a carrier gas of nitrogen is shown in Figure 3-6 for T_{High} = 300°C and T_{Low} = 100°C. Although the partial pressure increase for isotopes (for example, a dilute mixture of $C^{14}H_4$ in $C^{12}H_4$) is ~0.5%, a 10% concentration increase is common for constituents chemically different from the carrier gas [8]. This comparatively large partial pressure ratio makes it possible to concentrate a dilute constituent by many orders of magnitude, as will be discussed later.

Now consider the condition where the thermal gradient is imposed on a gas mixture having no constraining walls. In this case the constituents can diffuse without a concentration buildup at an average velocity V_{Soret}

$$V_{Soret} = \theta \frac{dT}{dx} = \frac{D_{12}\alpha_{12}}{T} \frac{dT}{dx}$$

(3.4)

where θ is the thermal diffusion velocity coefficient, D_{12} is the diffusion coefficient in the carrier gas, T is the temperature, and dT/dx is the thermal gradient. Both from calculations and experimental measurements, particles from 1 nm to 1 μm in diameter have nearly the same thermally driven diffusion coefficient, $\theta \approx 2.4 \times 10^{-4}$ cm^2 s^{-1} K^{-1} in nitrogen [9],[10]. This is because the time average force on a particle is just offset by its diffusion coefficient D_{12} so the product of D_{12} and α_{12} is nearly constant. For smaller constituents, <1 nm, the thermal force generated by a thermal gradient does not scale with size, but depends upon the details of the intermolecular interactions and approaches zero as the size and molecular weight of the dilute constituent approaches that of the carrier gas. Figure 3-7 shows the approximate thermal diffusion velocity coefficient for constituents as a function of size. To achieve a large Soret velocity, it is necessary to increase the thermal gradient. As will be discussed next, by using microlithographically patterned resistors, large thermal gradients, ~10^4 K cm^{-1}, can be generated which can result in Soret velocities of 1–30 cm s^{-1}.

16
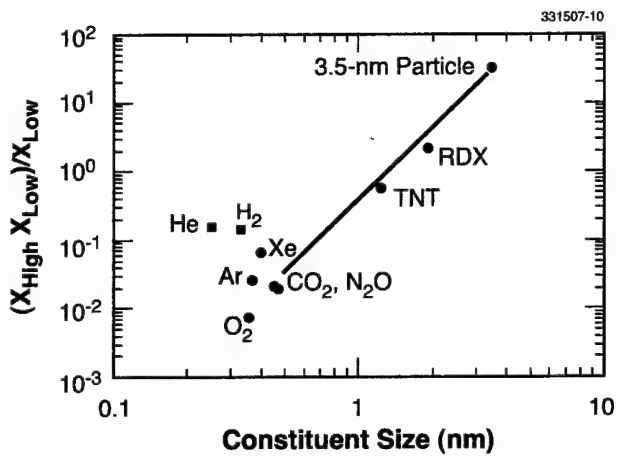
Figure 3-6. Normalized absolute concentration increase of dilute constituent between hot (300°C) and cold (100°C) regions in a nitrogen carrier gas. The square data points indicate constituents that concentrate in the hotter regions. Data for the explosive compounds TNT and RDX were estimated from the size of the molecules and by extrapolation of the curve between published data for CO_2 and N_2O and 3.5-nm particles in nitrogen.
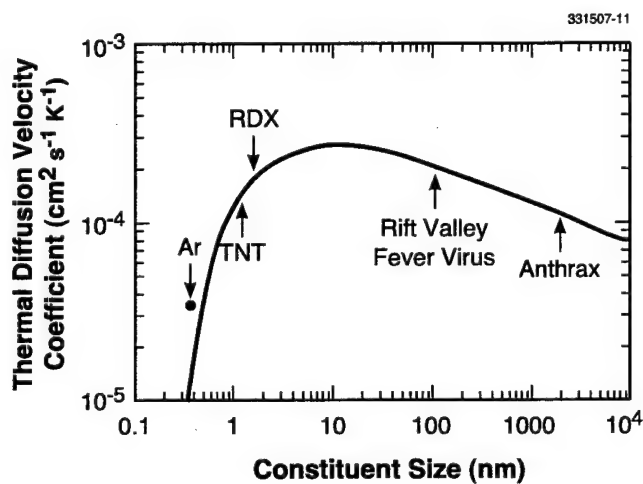
Figure 3-7. Thermal diffusion velocity coefficient in nitrogen as a function of particle size. The coefficients for RDX and TNT were estimated from the size of the molecules and by extrapolation of the thermal velocity curve between published data for CO_2 and N_2O and 3.5-nm particles in nitrogen.

17
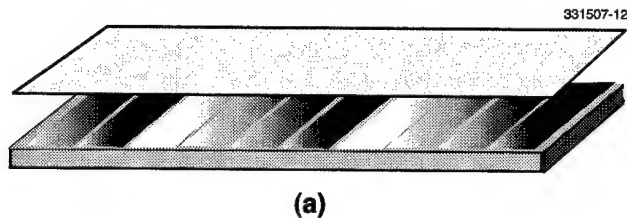
(a)
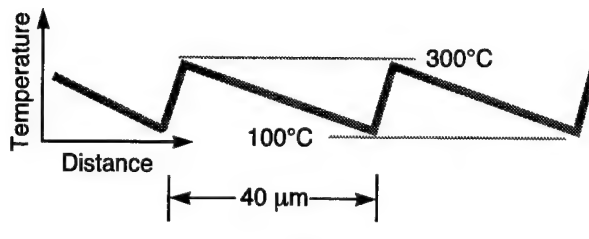
(b)

Figure 3-8. (a) A series of resistors represented by gray stripes are placed on the bottom side of a confined channel. Current through the resistors is used to generate a thermal sawtooth profile. The shading of each resistor represents its temperature, with lighter shades signifying higher temperatures. (b) The thermal profile from 100 to 300°C over a distance of ~40 µm was used to model the efficiency of the constituent concentration.
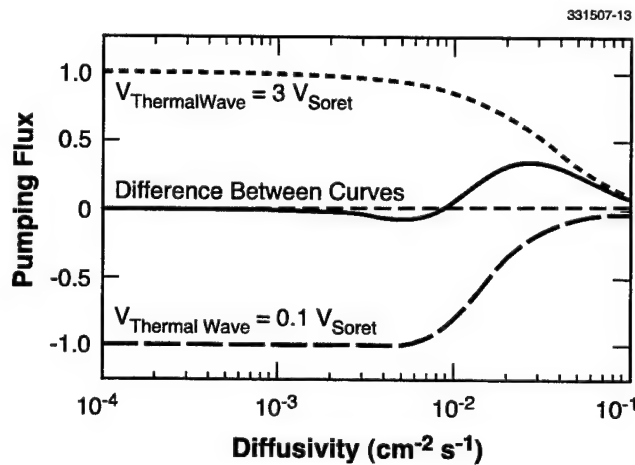
Figure 3-9. Normalized pumping flux as a function of diffusion coefficient D_{12}. The pumping flux is normalized to the pumping flux of a constituent with $D_{12} = 0$. The long-dashed curve is for the thermal velocity = 0.1 times the Soret velocity, pumping constituents to the left; and the short-dashed curve is for the thermal velocity = 3 times the Soret velocity, pumping constituents to the right. The solid curve is the difference of the short- and long-dashed curves, with the constituents of D_{12} with negative values being pumped to the left and constituents with positive values being pumped to the right.

18

Thermophoresis has been used to concentrate and separate isotopes by passing the gaseous constituents through a series of vessels in which thermal gradients are present [8]. Miniaturization of this separation technique enables new possibilities. The device we are proposing does not consist of a series of vessels. Instead, it comprises one long channel in which a series of resistive heaters, lithographically defined on a substrate, are used to establish a series of local thermal gradients, as shown in Figure 3-8. Sawtooth thermal gradients can be defined by passing different currents through the resistive elements. Constituents of higher molecular weight than the nitrogen carrier gas will concentrate in the cooler regions. Depending on the thermophoresis coefficient of the impurity, the degree of concentration can vary from ~10% to >10 times the average concentration, as indicated in Figure 3-6.

If the thermal velocity is below the thermal gradient driven Soret velocity, then the constituents with small D_{12} are concentrated in the colder regions of the sawtooth thermal profile and will move down the channel at the thermal velocity. Constituents with larger D_{12} are not concentrated to the same degree in the colder regions and their effective pumping velocity is less than the thermal velocity, as indicated by the long-dashed curve of Figure 3-9. When the thermal velocity approaches and exceeds the Soret velocity, constituents are no longer confined to the cold region and the effective constituent velocity in the channel is below the thermal velocity for constituents of both large and small D_{12}. In this case the constituent velocity flux becomes less dependent upon the D_{12}, as shown by the short-dashed curve in Figure 3-9. Since most constituents have the same Soret velocity, the distribution of a constituent in the channel will depend primarily upon D_{12} and the thermal velocity. Large particles with small D_{12} are easily concentrated in the colder regions, and small molecules with large D_{12} are more evenly distributed over the thermal gradient.

We have identified three variables—the thermal gradient of the sawtooth profile, the velocity of the thermal wave, and the direction of the thermal wave (pumping in or out of the channel)—that can be used to determine which constituents are concentrated in and which constituents are eliminated from the thermophoretic concentrator. One approach is suggested by the fact that increasing the thermal velocity above the Soret velocity increases the relative pumping flux of the higher diffusion constituents over the lower diffusion constituents, as shown by the short-dashed curve in Figure 3-9. If a thermal wave is moved to the right at three times the Soret velocity and then moved to the left at 0.1 times the Soret velocity (long-dashed curve in Figure 3-9), the net effect on the constituents in the channel is given by the solid curve shown in Figure 3-9. If the end of the channel is blocked, then the constituents that are pumped down the channel to the right will increase in concentration at the blocked end of the channel. The concentration will increase until the back diffusion comes into equilibrium with the pumping flux. Microfabrication techniques will enable the construction of a handheld concentrator with hundreds of segments that can produce thermal waves clocked at kilohertz rates. Such a device could produce concentration ratios of 10^5 in seconds while consuming a few watts of power.

M. W. Geis
R. R. Kunz

REFERENCES

1. C. A. Mack, *Inside PROLITH: A Comprehensive Guide to Optical Lithography Simulation* (FINLE Technologies, Austin, Tex., 1997).

2. F. H. Dill, W. P. Hornberger, P. S. Hauge, and J. M. Shaw, *IEEE Trans. Electron Devices* **ED-22**, 445 (1975).

3. C. A. Mack, T. Matsuzawa, A. Sekiguchi, and Y. Minami, *Proc. SPIE* **2725**, 34 (1996).

4. T. H. Fedynyshyn, S. P. Doran, and C. A. Mack, to be published in *Proc. SPIE* **3678** (1999).

5. L. Dufour, *Arch. Sci. Phys. Nat.* **26**, 546 (1872).

6. D. Enskog, *Phys. Z.* **12**, 533 (1911).

7. S. Chapman and F. W. Dootson, *Philos. Mag.* **33**, 248 (1917).

8. S. Chapman and T. G. Cowling, *Mathematical Theory of Non-Uniform Gases* (Cambridge University Press, New York, 1970), Chap. 14.

9. L. Waldmann and K. H. Schmitt, in *Aerosol Science*, C. N. Davies, ed. (Academic, New York, 1966), Chap. 6.

10. W. C. Hinds, *Aerosol Technology: Properties, Behavior, and Measurement of Airborne Particles* (Wiley, New York, 1982), Chap. 8.

4. BIOSENSOR AND MOLECULAR TECHNOLOGIES

4.1   RESPONSE OF ATTACHED B CELLS WITHIN A BIOELECTRONIC SENSOR

A new bioelectronic sensor is being developed for the project called CANARY (Cellular Analysis and Notification of Antigen Risks and Yields) and has been described in previous reports [1],[2]. The cornerstone of this sensor is a B-cell line which is derived from a white blood cell and which expresses antibodies on the outer membrane specific for a particular molecule (antigen). Antibody-antigen interaction generates a signal inside the B cell, which is amplified through a secondary messenger cascade, and results in an increase in internal calcium-ion concentration. We have engineered an immortal B-cell line to permanently express the jellyfish aequorin gene, which produces a calcium-activated protein that generates light in the presence of its substrate, coelenterazine. In this way, we have developed cells that emit photons in response to antigen binding.

We have previously demonstrated imaging of stimulated B cells flowing within a prototype microfluidic package. In these measurements B cells were not attached to any solid support but were instead freely suspended in solution. For implementation in a sensor, however, it would be desirable if these cells could be tethered down or directly attached to a solid support such as glass. We now report on results achieved using monolayers of B cells which have been attached to a glass substrate that forms one wall of a microfluidic channel. Attachment of this B-cell line to cleaned glass substrates occurs without additional surface modification treatments. If necessary, one can fabricate isolated patches of cells by using an additional patterned polydimethylsiloxane (PDMS) gasket layer to define the active sites.

In Figure 4-1, we demonstrate imaging of a patterned monolayer of B cells using an image-intensified charge-coupled device camera. Figure 4-1(a) is a reference image taken using an external light source transmitted through the device package. The serpentine structure of the microfluidic channel is evident. Cell sites defined by the PDMS gasket are highlighted by the dashed boxes. In this case, each cell site is a 2×2-mm-square glass surface which has been defined within the microfluidic channel. B cells were manually loaded at monolayer coverage into the lower four out of six available sites. Figure 4-1(b) shows imaging results (20-s exposure) after stimulation with 10^{-6} M anti-IgM, which is used to crosslink the B-cell receptors on the outside of the cell and thus generate a physiologically relevant signal. Background noise is predominantly due to speckle from the image intensifier. Additional scattering of B-cell-generated light is also visible in the image but does not appear to degrade sensor performance.

In Figure 4-2, we show dose-response behavior of attached cells, as measured using a photomultiplier tube, to demonstrate that cell attachment does not adversely affect cellular transduction of a binding event. This data set was taken with serpentine cell patterns defined by the microfluidic unit itself under stimulation concentrations of 10^{-6}, 10^{-7}, and 10^{-8} M anti-IgM. As in the case of unattached cells, peak times take longer to occur for the lower concentrations of stimulants. The sharp initial-peak amplitude decreases rapidly with stimulant concentration, with saturation occurring above approximately $10^{-6.5}$ M.

331507-14P
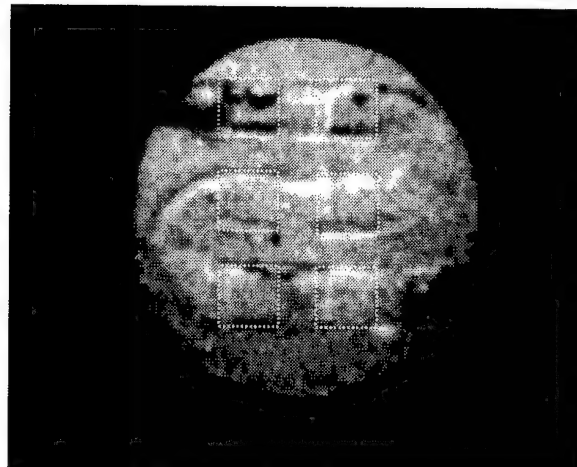
(a)
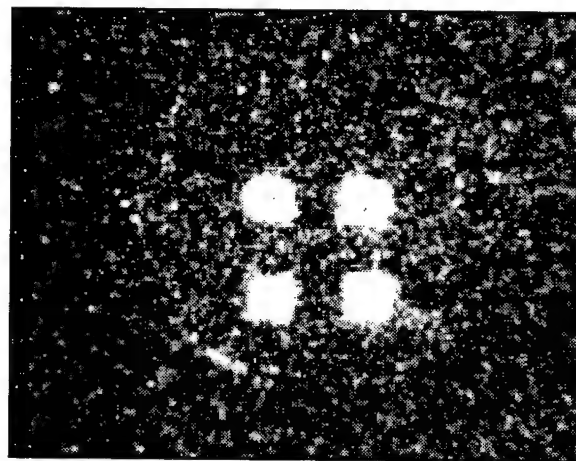
(b)

Figure 4-1. Imaging of a patterned monolayer of B cells using an image-intensified charge-coupled device camera: (a) reference image taken using an external light source and (b) results (20-s exposure) after stimulation with 10^{-6} M anti-IgM.

22
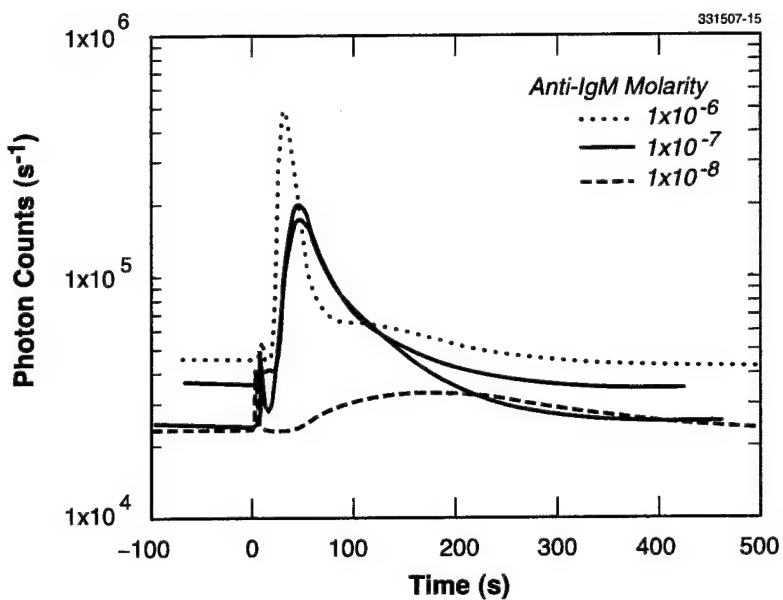
Figure 4-2. Dose-response behavior of attached cells, as measured using a photomultiplier tube, to demonstrate that cell attachment does not adversely affect cellular transduction of a binding event.

A later secondary peak is seen to have not as strong a dependence on stimulant concentration. When compared with similar test-tube-based experiments on unattached B cells, one sees very little effect of attachment on the cellular photonic response to stimulus.

A. M. Young   M. S. Petrovick
L. Parameswaran   T. H. Rider
L. T. Smith   R. H. Mathews
S. T. Palmacci   K. M. Molvar
M. A. Hollis   J. Chen

REFERENCES

1. Solid State Research Report, Lincoln Laboratory, MIT, 1998:4, p. 27.

2. Solid State Research Report, Lincoln Laboratory, MIT, 1999:1, p. 21.

5. MICROELECTRONICS

5.1 TRANSIENT ANALYSIS OF PHOTOGENERATED CHARGE-CARRIER COLLECTION IN HIGH-FRAME-RATE CHARGE-COUPLED DEVICES

A variety of interesting two-dimensional imaging applications require multiple sequential image acquisitions at submicrosecond frame times. To determine a detector's response to a rapidly varying optical signal, both the photogenerated carrier diffusion and drift characteristics must be evaluated. We report here on the simulated transient analysis of photocarrier collection by the wells of a charge-coupled device (CCD) pixel structure after exposure to a light pulse. The investigation included the evaluation of pixel structures with and without an electronic shutter [1]. Transient analysis of photogenerated carrier drift and diffusion effects was performed using a device simulator ATLAS and an optical ray trace simulator LUMINOUS to determine CCD pixel well spacing vs photocarrier collection times.

Figure 5-1 illustrates the transient analysis methodology used to determine the time required for carrier diffusion and/or drift to the collection wells after photogeneration. A short, narrow pulse of 420-nm light ramped to an intensity of 0.5 W cm^{-2} in 20 ns illuminates the wafer back side surface and is then turned off. The electron concentration in two collection wells, separated by a distance d (μm) and formed near the front side wafer surface by appropriate applied biases, is monitored, and the time to collect 99% of the photogenerated charge is recorded. The light is placed equidistant between the two collection wells for worst-case analysis. The inset shows that all of the charge is eventually collected in the wells.

Of particular interest in this analysis is a comparison of the charge collection dynamics of the conventional CCD structure to one containing an electronic "shutter" region. The "shuttered" device is characterized by a region of high concentration of p-type dopant formed approximately 2 μm below the wafer surface. This region is formed by a high-energy (>1.5 MeV) implantation. The phototransient analysis was performed for identical test structures both with and without this shutter implant.

Figures 5-2(a) and 5-2(b) illustrate hole concentration contours for the shuttered and unshuttered test structures, respectively, with appropriate positive biases applied to the two collection electrodes (the collection electrodes are 10 μm in width located at the wafer surface and separated by 30 μm for the case shown). The red areas show the extent of the depletion region for both cases. Note that the shutter p barrier region, shown in Figure 5-2(a), effectively prevents the depletion region from expanding into the substrate under the middle (noncollecting) electrode between the two collecting electrodes. For the unshuttered case the depletion region extends deeply into the bulk. Electrons, which reach the depleted zone by diffusion, will rapidly drift to the collection wells under the influence of the electric field.

Figures 5-3(a) and 5-3(b) illustrate electron concentration contours (photogenerated charge) for the shuttered and unshuttered structures, respectively, after 20 ns of illumination but just before being extinguished. The contours illustrate the flow of electrons to the collection wells. Note how the shuttered device, shown in Figure 5-3(a), prevents charge from reaching the wafer surface under the noncollecting electrode. By contrast to the shuttered case, the electrons in the unshuttered structure flow predominantly to the front
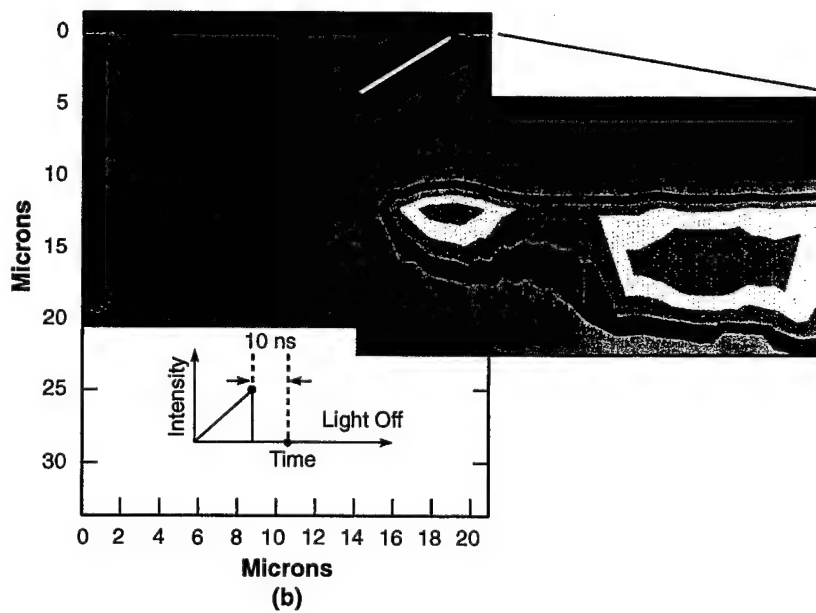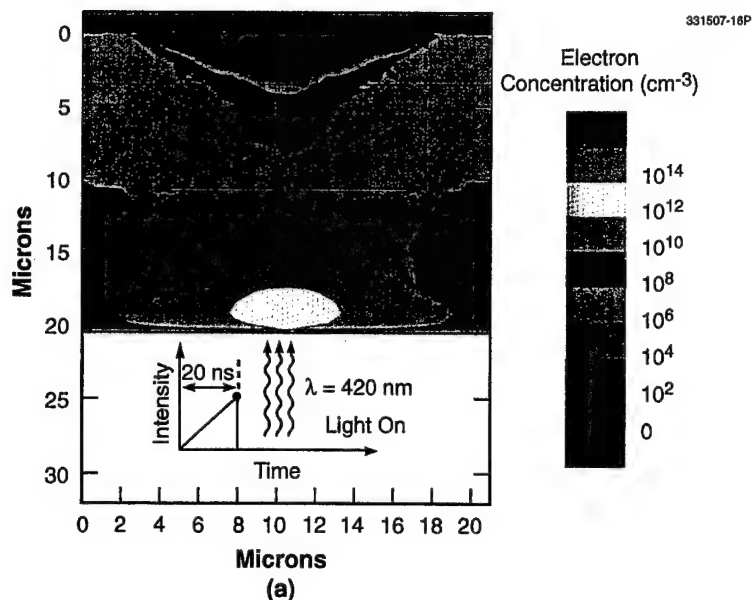
Figure 5-1. Summary of the transient analysis methodology. Electron concentration contours are plotted during a (a) light-on, (b) light-off sequence, and total collected charge is monitored as a function of time. Collection electrodes located on the front side surface are 10 µm in width separated by a distance d (µm). The inset shows that all of the charge is eventually collected in the well.

26

331507-17P

(a)

(b)

Hole Concentration (cm^{-3})

10^{18}

10^{15}

10^{12}

10^{9}

10^{6}

10^{3}

0
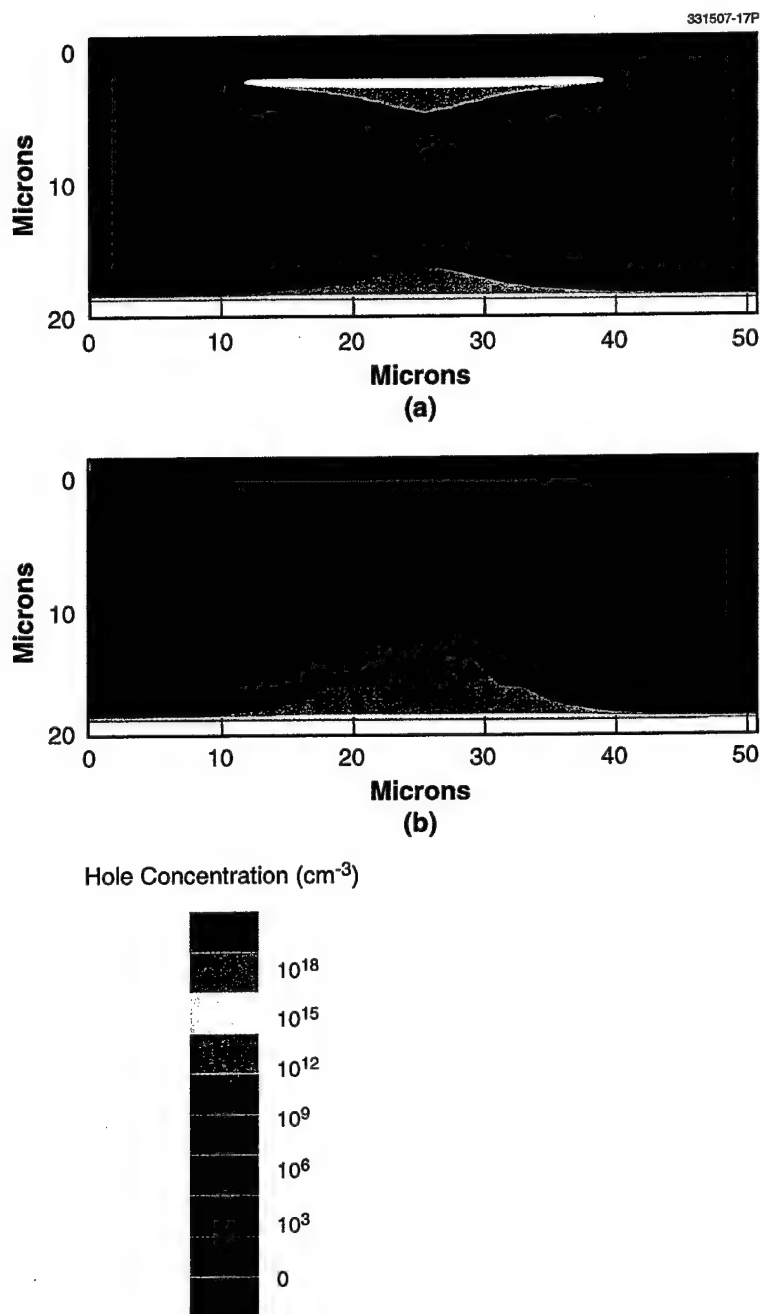
Figure 5-2. (a) Hole concentration contours for electronically shuttered devices with collection electrodes at large positive biases. Electrode separation is 30 μm. (b) Hole concentration contours for unshuttered device of the same geometry and bias as in (a).

27

331507-18P
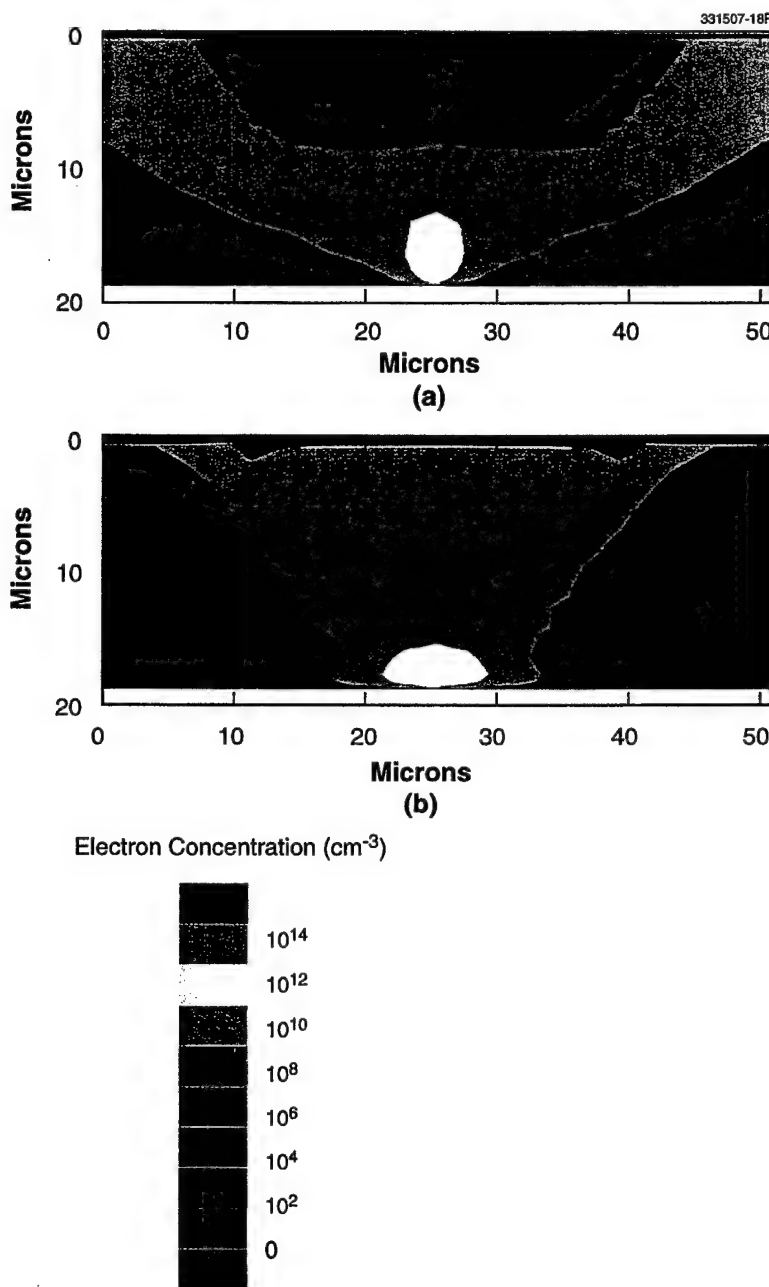
Figure 5-3. (a) Electron concentration contours for shuttered device of Figure 5-2(a) at the moment the light has been on for exactly 20 ns. (b) Electron concentration contours for the unshuttered device of Figure 5-2(b) under the same illumination conditions described in (a).

28
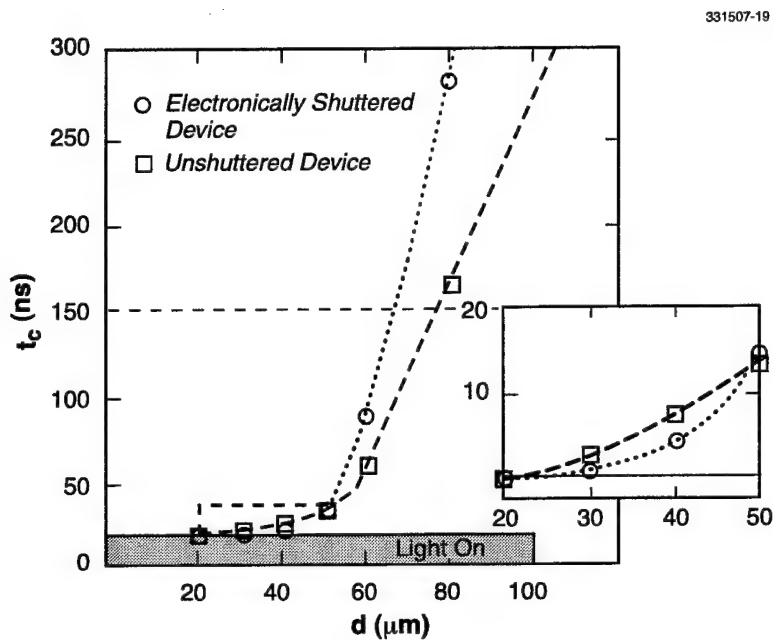
Figure 5-4. Time to collect 99% of the photogenerated electrons, t_c, vs collection electrode separation d for both shuttered and unshuttered device structures.

surface under the noncollecting electrode. Once in the wells at the front side, the charge diffuses to one of the collection wells along a quasi-one-dimensional path. The total charge collected in each well was monitored as a function of elapsed time during the light-on, light-off sequence. These simulations were then repeated for both shuttered and unshuttered device structures where the collection electrode separation was varied from 20 to 100 μm.

Figure 5-4 shows the time to collect 99% of the photogenerated electrons, t_c, as a function of collection electrode separation obtained for the shuttered and unshuttered device structures as described above. Note that for an electrode separation of 50 μm or less all of the photogenerated charge is collected in less than 50 ns after the light is extinguished. For separation distances greater than approximately 60 μm, the collection time increases dramatically. The data also show that the shuttered device is slightly faster in charge collection than the unshuttered device for electrode separations less than 50 μm, but is dramatically slower than the unshuttered device for larger separations. This is fundamentally related to the differences in the drift/diffusion paths for the two structures and is explained as follows: For small collection electrode separations (<50 μm), where the depletion regions from the two electrodes nearly overlap, most of the photogenerated charge is rapidly collected in the two wells for both structures. In the unshuttered device, however, a residual amount of charge goes to the surface under the middle electrode where it then moves more slowly by diffusion along the surface to the collection wells. For large collection electrode separations (>60 μm), the undepleted region in the shuttered device becomes relatively wide, and diffusion in this neu-

29

tral region dominates the collection time. For the unshuttered device, the photogenerated electrons are quickly attracted to the surface by the electric field that extends deep into the bulk. Though the electrons still have to diffuse to the collection wells, this process is faster (compared to the shuttered case) because of the very high electron concentration gradient and the nature of one-dimensional diffusion in the CCD buried channel.

<div align="center">D. D. Rathman</div>

<div align="center">

REFERENCE

</div>

1. R. K. Reich, R. W. Mountain, W. H. McGonagle, J. C-M. Huang, J. C. Twichell, B. B. Kosicki, and E. D. Savoye, *IEEE Trans. Electron Devices* **40**, 1231 (1993).

6. ANALOG DEVICE TECHNOLOGY

6.1 MAGNETICALLY TUNABLE SUPERCONDUCTING FILTERS

Tunable filters are an important element of the rf front end of electronic warfare, frequency-agile radar, and communications systems. Many surveillance and radar receivers in use today employ filters that are based on magnetically tunable resonators made from yttrium-iron-garnet (YIG) ferrite spheres [1]. In some cases these filters can be tuned over more than one octave, but they can only be tuned either relatively slowly (milliseconds) or with high-energy circuits. YIG filters also have limited power-handling capabilities because of a low threshold for nonlinear behavior due to generation of spin waves.

In the last few years, high-performance, very low loss fixed-frequency filters utilizing high-transition-temperature superconductor thin films have been developed [2]. These filters, often in combination with cooled low-noise amplifiers, can improve the performance of many microwave systems. Filters with similar characteristics, and with the added advantage of fast tunability, would combine the improved sensitivity and selectivity with the agility required in many microwave systems.

We have previously reported [3],[4] results from measurements on tunable resonators showing that high Q's and adequate tunability are achievable. The large values of figure of merit for resonators indicate that high-performance filters should be realizable. A three-pole Chebyshev filter was chosen for demonstrating the capabilities of the superconductor/ferrite technology. The design bandwidth was 1% at a center frequency of 10 GHz. The microstrip geometry was used incorporating coupled resonators one half-wavelength long ($\lambda/2$) at resonance. The design is complex enough to demonstrate the potential of tunable filters with this technology, but small enough to fit on available substrates. A linear design using end-coupled resonators was used in order to minimize changes in coupling caused by changes of the effective permeability. Electric fields are primarily responsible for the coupling in this geometry, so effects of the changes in permeability on the resonator coupling are minimized. For reasons of simplicity, all of the tuning for the filters reported here was performed in an external coil which generates the magnetic field used for the tuning.

For the first demonstrations, niobium superconductor was chosen because of the simplicity of fabrication. Niobium can be deposited directly on the ferrite, while the high-T_c materials require epitaxial growth on lattice-matched substrates, ruling out direct deposition on ferrite. We fabricated a filter using linear, end-coupled, $\lambda/2$, niobium resonators on G1210 ferrite and on polycrystalline YIG. A niobium ground plane was used. The filter was operated at 4 K. Figure 6-1 shows schematically the layout of the filter.

Figure 6-2 shows the results of the measurements of the filter insertion loss (S_{21}) vs frequency for a number of applied external magnetic fields. The magnetic field ranges from zero (unmagnetized substrate) for the lowest frequency passband up to the maximum shown which is 300 G for the highest frequency passband. The tunable range shown is approximately 800 MHz, giving a tunability of 8%. Above 300 G the filter response begins to degrade; the insertion loss increases and the shape becomes more rounded. The degradation of the passband results from decreases in the resonator Q and changes in the resonator coupling as the center frequency moves. The insertion loss shown is about 1 dB. The calculated

31

331507-20

Niobium

Ferrite
Magnetization
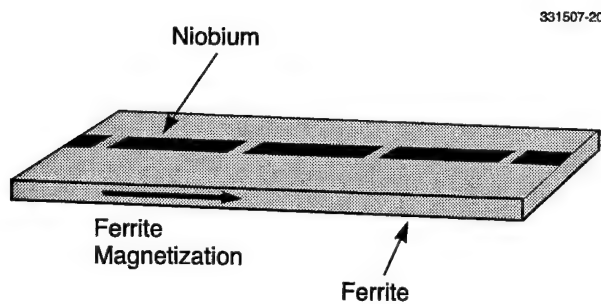
Ferrite

Figure 6-1. Schematic view of tunable filter, showing niobium resonators on the ferrite substrate. The coil for providing the magnetization is not shown.

331507-21
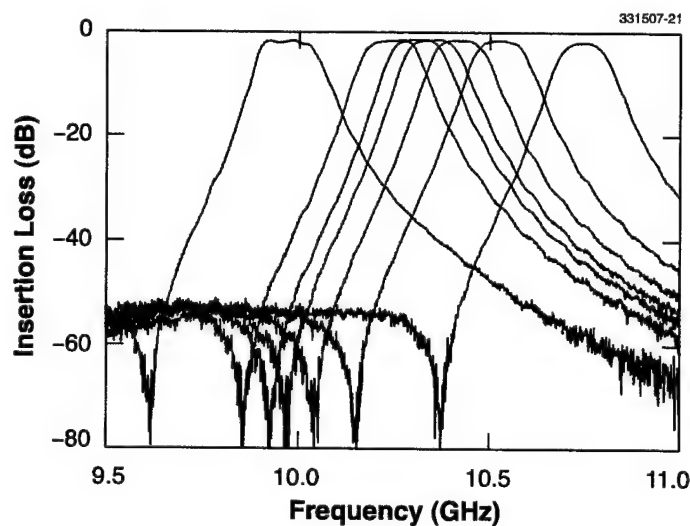
Figure 6-2. Insertion loss vs frequency for the filter of Figure 6-1, for several values of applied magnetic field from zero to approximately 300 G. The materials are niobium superconductor on G1210.
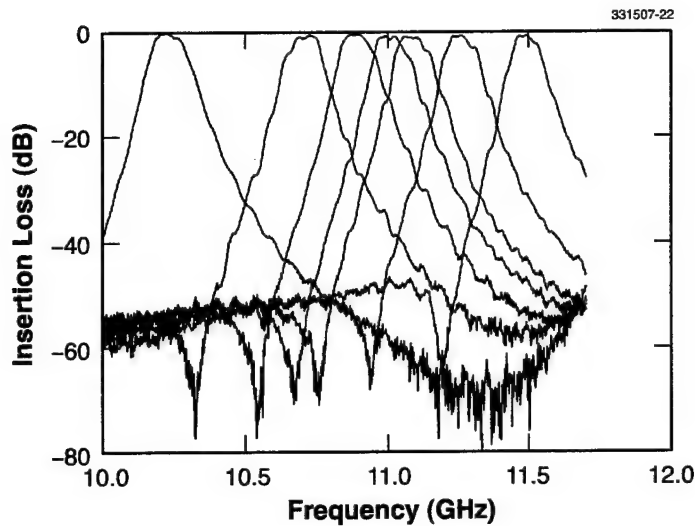
Figure 6-3. Insertion loss vs frequency for the filter of Figure 6-1 using polycrystalline YIG (Trans Tech G113) for the ferrite material and niobium superconductor. Note the wider frequency scale than in Figure 6-2.

insertion loss is less than 0.1 dB based on the previously measured Q of ~5000 for a niobium $\lambda/2$ resonator fabricated on this substrate material [3]. We are investigating the source of the additional loss, which could be from higher losses on this particular substrate or from parasitic losses due to variations in connectors or packaging.

Figure 6-3 shows the insertion loss vs frequency for a filter fabricated on polycrystalline ferrite YIG, which has a larger saturation magnetization and therefore a larger tunability [5]. For the same applied fields as with G1210, we obtain approximately 13% tunability. The losses are well below 1 dB, lower than for G1210 because it is believed that the YIG has lower losses.

As discussed above, it is not possible to deposit $YBa_2Cu_3O_{7-\delta}$ (YBCO) or other high-T_c materials directly on ferrite substrates, because the film must be grown epitaxially on a lattice-matched substrate to obtain low microwave losses. However, biaxially oriented buffer layers can be deposited on ceramic and polycrystalline substrates by the ion-beam-assisted deposition (IBAD) process [6]. Epitaxial YBCO with low microwave losses can then be deposited on the IBAD layer by any convenient process such as laser ablation or sputtering [7].

Figure 6-4 shows schematically the filter fabricated from IBAD YBCO on the polycrystalline ferrite YIG with a yttria-stabilized zirconia (YSZ) buffer layer as described in [7]. This is the same design and layout used for the niobium filter. The differences in dielectric constant were expected to be small enough that no adjustments of the design were needed. Figure 6-5 shows the measurement of the filter insertion

33

331507-23
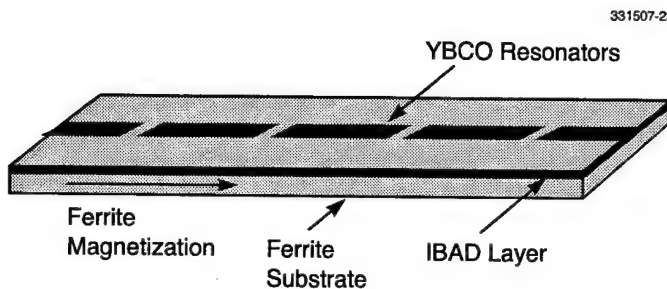
Figure 6-4. Schematic view of filter fabricated from ion-beam-assisted deposited (IBAD) YBCO. The IBAD buffer layer is YSZ.
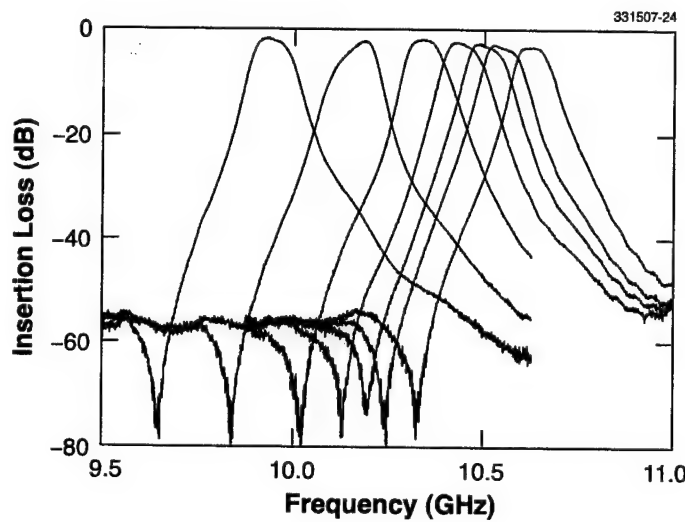
Figure 6-5. Insertion loss vs frequency of IBAD YBCO on a polycrystalline YIG ferrite substrate. The temperature was 77 K and the input power was –10 dBm.

loss vs frequency at 77 K for approximately the same values of the externally applied magnetic field, as shown in Figure 6-3. The tunability of 10% is consistent with the filter on YIG with niobium resonators when account is made for the lower saturation magnetization of the YIG at 77 K compared with 4 K [5]. The input power was –10 dBm. The insertion loss in the unmagnetized state is about 2 dB, which is larger than expected from the surface resistance measured previously in the unpatterned IBAD YBCO [7]. The causes of the increased insertion loss are under investigation.

34

331507-25
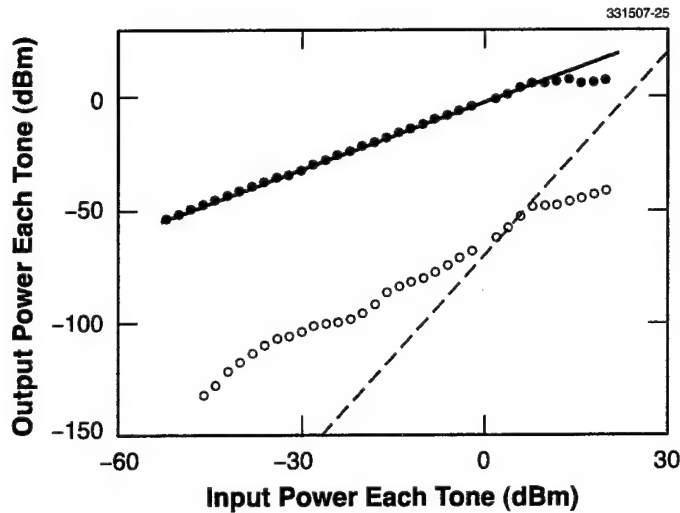
Figure 6-6. Results of third-order intermodulation measurements on the filter of Figure 6-1. The materials are niobi-um on G1210. These results are for the filter in the unmagnetized state. The two-tone separation is 1.96 MHz at 10.3 GHz. The dashed line shows slope three in order to estimate the third-order intercept.

Power handling and linearity are important performance measurements of tunable filters for the potential applications that have been discussed here. The linearity of the front-end filter can set the dynamic range of the entire system. We have carried out standard two-tone, third-order intermodulation (IM) measurements using the filter of Figure 6-1 using G1210 ferrite. The result is shown in Figure 6-6. At the input power of +8 dBm the third-order IM products are nearly 60 dB below the fundamental. This is a low value of IM distortion and indicates that the power handling of the filter is adequate for many applications. Above +10 dBm the filter insertion loss increases and the output power saturates. This is probably due to the niobium superconductor as a similar effect was observed in an identical fixed-tuned filter fabricated on a ceramic substrate.

It may be anticipated that the power handling could be superior to that of standard YIG filters (approximately +10 dBm) because the polycrystalline material used has a larger ferrimagnetic-resonance linewidth than single-crystal YIG, and the threshold rf magnetic field for excitation of spin waves is higher than in the case of conventional YIG filters. The third-order products in Figure 6-6 do not have a slope of three as would be expected but this is often seen for superconducting filters. It is not understood why the IM products fail to show a slope of three [8]. The IM products shown are probably resulting from the superconductor. The deviation from slope three makes it difficult to quote a value for the third-order inter-cept (IP3). We can however estimate that it is near +40 dBm.

Intermodulation has not yet been measured in the IBAD YBCO filter. The power handling, however, showed no degradation of the filter response up to +5-dBm input power, the highest that was measured. The IM measurements on the YBCO filters are in progress.

We have demonstrated a compact superconducting/ferrite filter with useful tuning range of $\Delta f/f \approx$ 10% and insertion loss <1 dB using niobium superconductor. We have also demonstrated a filter using IBAD-deposited YBCO as the superconductor. The IBAD filter demonstrated the expected tunability, and further efforts are under way to optimize the process to reduce losses. The results reported here strongly indicate that high-performance tunable filters can be fabricated that operate at 77 K. The niobium devices have excellent linearity IP3 $\approx$ 40 dBm, and power-handling capability >10 dBm. This technology can utilize low-energy tuning circuits and be rapidly tuned, as we have demonstrated in previous work [9].

D. E. Oates   G. F. Dionne
P. N. Arendt*   R. F. DePaula*
J. R. Groves*   S. R. Foltyn*
Q. X. Jia*

REFERENCES

1.   J. Helszajn, *YIG Resonators and Filters* (Wiley, New York, 1985).

2.   M. J. Lancaster, *Passive Microwave Device Applications of High Temperature Superconductors* (Cambridge University Press, Cambridge, 1997).

3.   D. E. Oates and G. F. Dionne, *International Conference on Measurements for Telecommunication Transmission Systems (MTTS) Digest* (Institution of Electrical Engineering, London, 1997), p. 303.

4.   Solid State Research Report, Lincoln Laboratory, MIT, 1997:3, p. 35.

5.   G. F. Dionne and D. E. Oates, *IEEE Trans. Magn.* **33**, 3421 (1997).

6.   A. T. Findikoglu, S. R. Foltyn, P. N. Arendt, J. R. Groves, Q. X. Jia, E. J. Peterson, X. D. Wu, and D. W. Reagor, *Appl. Phys. Lett.* **69**, 1626 (1996).

7.   Q. X. Jia, A. T. Findikoglu, P. Arendt, S. R. Foltyn, J. M. Roper, J. R. Groves, J. Y. Coulter, Y. Q. Li, and G. F. Dionne, *Appl. Phys. Lett.* **72**, 1763 (1998).

8.   B. A. Willemsen, T. Dahm, and D. J. Scalapino, *Appl. Phys. Lett.* **71**, 3898 (1997).

9.   D. E. Oates and G. F. Dionne, to be published in *IEEE Trans. Appl. Supercond.*

*Author not at Lincoln Laboratory.

7. ADVANCED SILICON TECHNOLOGY

7.1 HIGH-SPEED TEST RESULTS OF 0.25-μm FULLY DEPLETED SILICON-ON-INSULATOR CMOS TECHNOLOGY

A data generation/acquisition circuit (DGAC) test chip, designed by Mayo Foundation, has been fabricated using Lincoln Laboratory's fully depleted silicon-on-insulator (FDSOI) CMOS process [1]. This process uses 0.25-μm n and p dual-doped polysilicon gates and fully planar three-level metal interconnects. Self-aligned Co-silicide was formed on top of the polysilicon gate and the source/drain ohmic contacts to reduce the resistance. The stage delay of a ring oscillator is 25 ps with a 2.5-V supply voltage and the cutoff frequency of the n-channel MOSFET is in the vicinity of 30 GHz.

The circuit block diagram of the DGAC test chip is shown in Figure 7-1. Various basic building blocks for signal processing, such as a shift register, pulse generator, frequency divider, control decoder, counter, multiplexer, variable delay, and trigger circuits, are implemented in Mayo's DGAC chip. The circuit consists of over 3600 internal logic gates with 14 000 FETs and 85 input/output bonding pads. To benchmark the speed of the FDSOI technology, a shift register consisting of D-type flip flops and a 6-bit logic circuit consisting mostly of NAND gates were tested. With a 2-V supply voltage, the maximum operating frequency is 1.75 GHz for the shift register and 1.2 GHz for the logic circuit.

One of the subcircuits is a 12-bit counter, consisting of approximately 400 logic gates, used to study the power dissipation of the CMOS circuits. The plot in Figure 7-2 shows the total power dissipation as a function of operating frequency. If 80% of the gates switch state per clock cycle, the dynamic power of the FDSOI technology is approximately 0.055 μW/MHz/gate, which is approximately 5 times lower than that of circuits fabricated with 0.25-μm bulk CMOS technology.

The waveforms of a buffer-stage test circuit measured at different supply voltages are shown in Figure 7-3. The maximum operating frequency is defined as the frequency at which the amplitude of the output signal is equal to half of the supply voltage. At 2-V supply voltage, the 950-MHz operating frequency is comparable to the 1 GHz of a similar GaAs circuit, but the 42-mW power dissipation is more than 40 times lower. When the supply voltage is lowered to 0.7 V, the circuit still functions at 200 MHz with a power dissipation of a mere 1.4 mW. This circuit demonstrates that at a similar switching speed, the FDSOI has a significant power advantage over other technologies. In a second buffer design in the DGAC test chip, the circuit size is significantly reduced, resulting in much shorter interconnects and distances of the buffer circuits to the probing pads. As a result, the operating frequency almost doubles to 1.8 GHz.

The test results demonstrated the speed and power-dissipation advantages of the FDSOI process and the potential of large-scale integration using this technology. Because of the high speed of the CMOS devices, the effect of interconnects becomes important and has to be carefully designed.

J. A. Burns   C. L. Cheng
C. K. Chen   J. M. Knecht
D. R. Yost

REFERENCE

1. J. A. Burns, C. L. Keast, J. M. Knecht, R. R. Kunz, S. C. Palmateer, S. Cann, A. Soares, and D. C. Shaver, *Proceedings of IEEE International SOI Conference* (IEEE, Piscataway, N.J., 1996), p. 102.
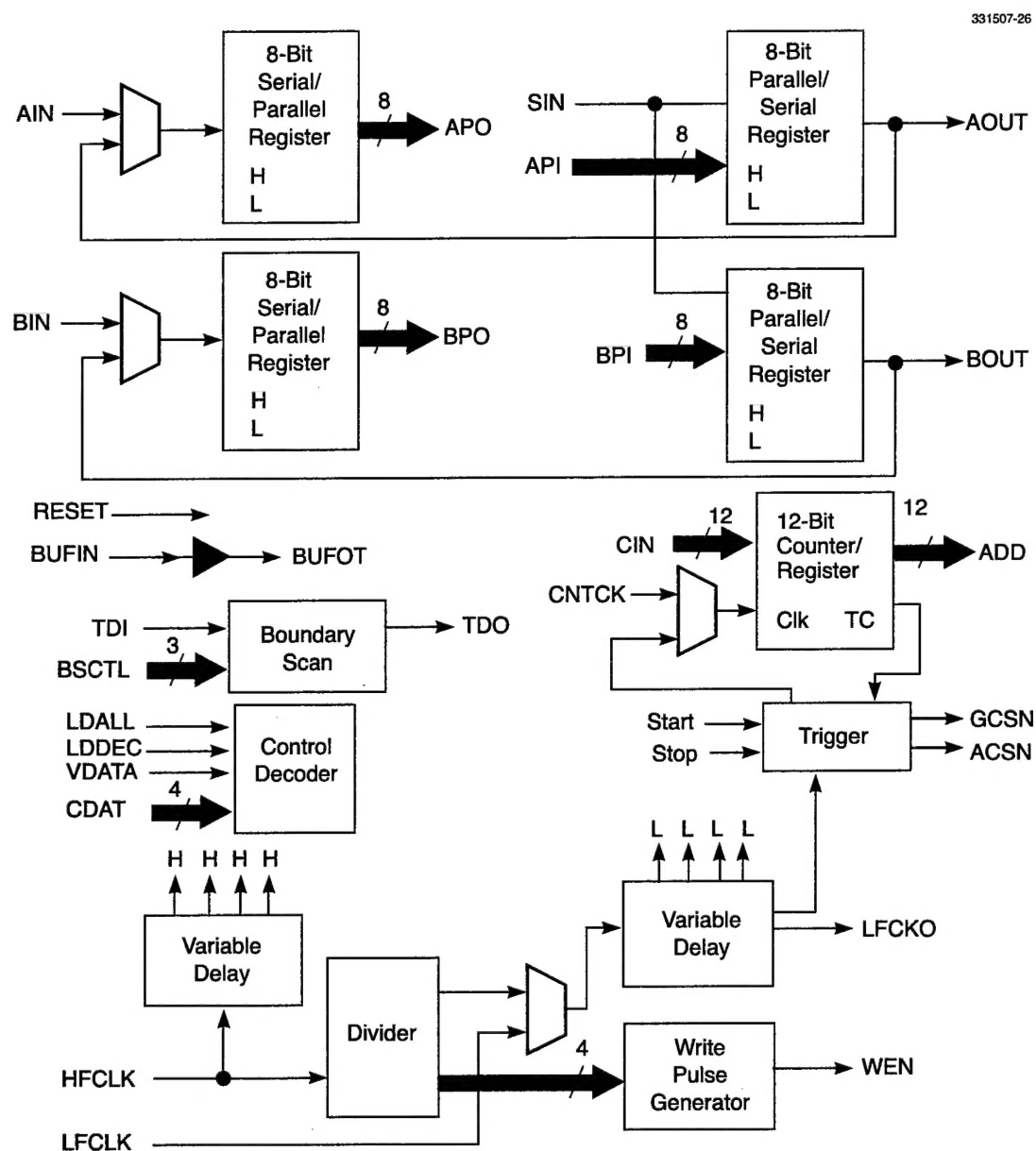
Figure 7-1. Circuit block diagram of the data generation/acquisition circuit (DGAC) test chip, consisting of 3610 gates, 49 inputs, and 36 outputs.
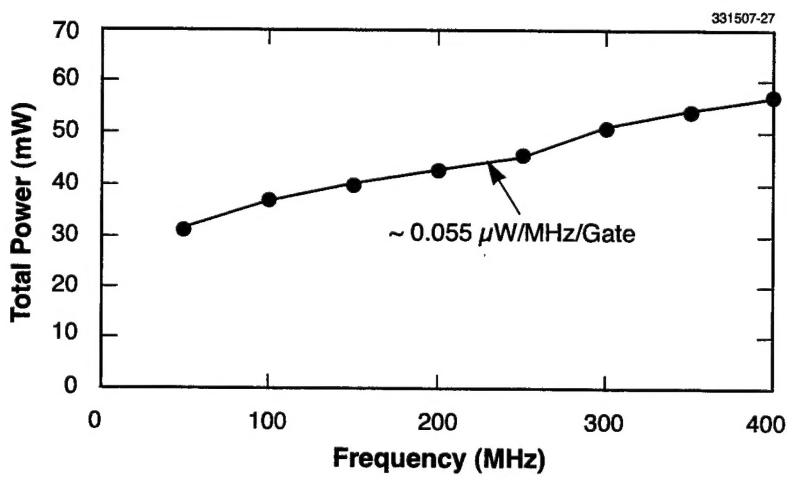
Figure 7-2. Total power dissipation as a function of the operating frequency for 12-bit counter subcircuit.
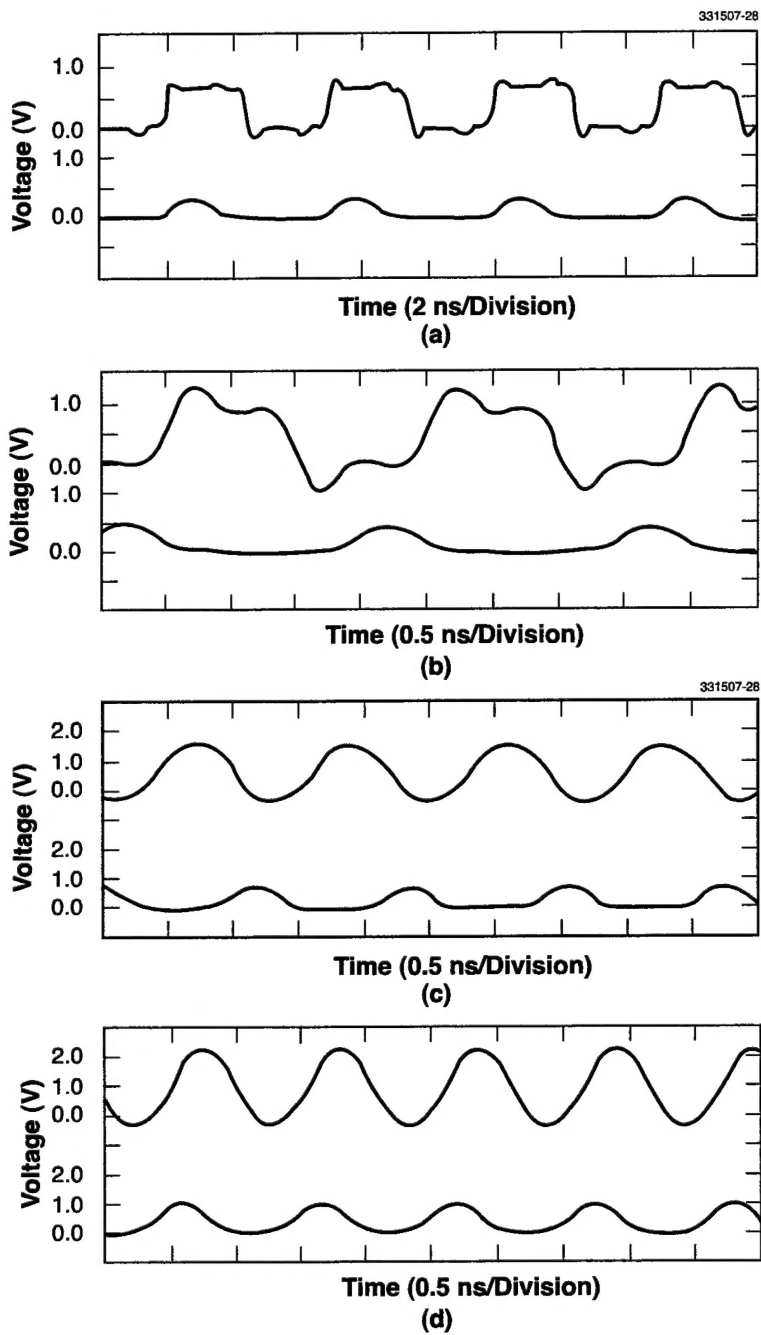
Figure 7-3. Input (upper) and output (lower) waveforms of buffer-stage test circuit measured at different supply voltages: (a) $V_{DD} = 0.7$ V, 2.1 mA, 200-MHz maximum; (b) $V_{DD} = 1.0$ V, 5.8 mA, 500-MHz maximum; (c) $V_{DD} = 1.5$ V, 12.8 mA, 840-MHz maximum; and (d) $V_{DD} = 2.0$ V, 21.3 mA, 950-MHz maximum.

41

REPORT DOCUMENTATION PAGE

1. AGENCY USE ONLY (*Leave blank*)	2. REPORT DATE 15 May 1999	3. REPORT TYPE AND DATES COVERED Quarterly Technical Report, 1 February–30 April 1999

4. TITLE AND SUBTITLE

Solid State Research

5. FUNDING NUMBERS

C — F19628-95-C-0002

6. AUTHOR(S)

David C. Shaver

7. PERFORMING ORGANIZATION NAME(S) AND ADDRESS(ES)

Lincoln Laboratory, MIT
244 Wood Street
Lexington, MA 02420-9108

8. PERFORMING ORGANIZATION REPORT NUMBER

1999:2

9. SPONSORING/MONITORING AGENCY NAME(S) AND ADDRESS(ES)

HQ Air Force Materiel Command
AFMC/STSC
Wright-Patterson AFB, OH 45433-5001

10. SPONSORING/MONITORING AGENCY REPORT NUMBER

ESC-TR-98-067

11. SUPPLEMENTARY NOTES

None

12a. DISTRIBUTION/AVAILABILITY STATEMENT

Approved for public release; distribution is unlimited.

12b. DISTRIBUTION CODE

13. ABSTRACT (*Maximum 200 words*)

This report covers in detail the research work of the Solid State Division at Lincoln Laboratory for the period 1 February–30 April 1999. The topics covered are Quantum Electronics, Electro-optical Materials and Devices, Submicrometer Technology, Biosensor and Molecular Technologies, Microelectronics, Analog Device Technology, and Advanced Silicon Technology. Funding is provided by several DoD organizations — including the Air Force, Army, BMDO, DARPA, Navy, NSA, and OSD — and also by the DOE, NASA, and NIST.

14. SUBJECT TERMS

quantum electronics, electro-optical devices, materials research, submicrometer technology, biosensor technology, microelectronics, analog device technology, advanced silicon technology, semiconductor lasers, tapered-amplifier power splitters, lithography modeling, superconducting filters, bioelectronic sensors, charge-coupled devices, data generation/acquisition circuit

15. NUMBER OF PAGES

67

16. PRICE CODE

17. SECURITY CLASSIFICATION OF REPORT	18. SECURITY CLASSIFICATION OF THIS PAGE	19. SECURITY CLASSIFICATION OF ABSTRACT	20. LIMITATION OF ABSTRACT
Unclassified	Same as Report	Same as Report	Same as Report